

# Melting of nano-PCM inside a cylindrical thermal energy storage system: Numerical study with experimental verification



Soroush Ebadi, Syeda Humaira Tasnim, Amir A. Aliabadi, Shohel Mahmud\*

School of Engineering, University of Guelph, Guelph, ON, Canada

## ARTICLE INFO

### Keywords:

Thermal energy storage system  
Phase change material  
Latent heat  
Numerical investigation  
Thermal conductivity enhancement  
Nanoparticles

## ABSTRACT

In the current work, the melting process, heat transfer, and energy storage characteristics of a bio-based nano-PCM in a vertical Cylindrical Thermal Energy Storage (C-TES) system are numerically investigated and verified with experimental work. Mathematical models based on non-linear differential equations are developed to study the mass, momentum, and energy transport processes inside the C-TES system. The effects of nanoparticles volume fraction (i.e.  $\phi = 0\%$ ,  $3\%$ , and  $5\%$ ) and Rayleigh number (i.e.  $Ra_{nl} = 10^6$ ,  $10^7$ , and  $10^8$ ) on the melting process are investigated. To compare the numerical results, an experimental setup is developed and transient images are captured to identify the location and shape of solid-liquid interface. To prepare nano-PCM, the copper oxide (CuO) nanoparticles are dispersed into the bio-based coconut oil PCM. The C-TES system is insulated from the bottom, isothermally heated from its lateral walls and the top. Numerically obtained solid-liquid interface locations and melt fractions for base PCM and nano-PCM are compared with experimental analysis and a very good agreement is obtained. The numerical results are further compared with existing numerical and experimental results available in the literature. The work then explains the effects of Rayleigh number and volume fraction of nanoparticles on melt fraction, Nusselt number, and stored energy. The results indicate that adding nanoparticles do not change the patterns of melt fraction, Nusselt number, and energy storage capacity with time compared to the base PCM case. The effects of specific heat capacity of solid nano-PCM, liquid nano-PCM, and latent heat capacity of nano-PCM on energy stored are discussed. The results show that the difference in energy stored with Rayleigh number is less during the beginning of the melting; as melting reaches in the convection dominated regime, a larger difference is observed due to increased melting at larger Rayleigh number.

## 1. Introduction

The ongoing increase in the worldwide population and industrial units is accompanied by a significant demand for energy. On the other hand, the limitation in the sources of conventional fossil fuels and the environmental issues associated with their uses, have caused several concerns and challenges such as security of energy supply and global climate change [1–4]. To overcome these issues, exploitation of renewable energies (e.g. solar energy, geothermal, wind energy, etc.) has been significantly considered by energy suppliers. However, due to the fluctuations and inability to control the sources of the renewable energies, it is more efficient for these systems to be used with energy storage systems [5]. Thermal Energy Storage (TES) systems are developed with an aim to store thermal energy in an efficient and reliable manner. TES systems have been used in a wide range of applications for heating/cooling purposes including building thermal management, food processing applications, Heating, Ventilation, and Air Conditioning (HVAC) systems, and solar power plants for storing thermal

energy during the day and release it during the night and cloudy days. In general, TES systems are divided into three main groups: sensible, latent, and thermo-chemical heat storage. Due to the effective use of Phase Change Materials (PCM) in improving Latent Heat Thermal Energy Storage (LHTES) systems, more impetus has been provided by researchers to develop the LHTES system with PCMs. Utilizing PCMs in LHTES systems have provided advantages of high energy density and an almost constant operating temperature [6]. In these systems, thermal energy is stored during the melting process and released during the solidification process. A wide range of PCMs with various melting temperatures including Paraffin waxes, organic and non-organic compounds, and hydrated salts are available for use in LHTES systems. Comprehensive information regarding different types of PCMs is available in [7]. To select a proper PCM, different parameters including phase change temperature, stability, amount of latent heat, and thermal conductivity should be considered [8]. Although having desirable attributes for storing thermal energy, PCMs suffer from low thermal conductivity, which results in a lower melting/solidification rate and

\* Corresponding author.

E-mail address: [smahmud@uoguelph.ca](mailto:smahmud@uoguelph.ca) (S. Mahmud).

Nomenclature			
$c_p$	specific heat at constant pressure [kJ/kg K]	$l$	liquid PCM
$g$	gravitational acceleration [m/s <sup>2</sup> ]	$m$	melt
$H$	height of the filled nano-PCM [cm]	$n$	nanoparticles
$h_{nl}$	latent heat of fusion [kJ/kg]	$nl$	liquid nano-PCM
$k$	thermal conductivity [W/m·K]	$ns$	solid nano-PCM
$R$	inner radius of the C-TES system [cm]	$s$	solid PCM
$T$	temperature [°C]	$0$	initial
<b>Greek symbols</b>		<b>Abbreviation</b>	
$\alpha$	coefficient of thermal diffusivity [m <sup>2</sup> /s]	C-TES	cylindrical thermal energy storage system
$\beta$	coefficient of thermal expansion [1/K]	TES	thermal energy storage
$\mu$	dynamic viscosity [Pa·s]	LHTES	latent heat thermal energy storage system
$\rho$	density [kg/m <sup>3</sup> ]	MF	melting fraction
$\phi$	volume fraction of nanoparticles	PCM	phase change material
<b>Subscripts</b>		RT	Rubitherm ( <a href="http://www.rubitherm.eu">www.rubitherm.eu</a> )
$h$	hot	$Ra_{nl}$	Rayleigh number based on liquid nano-PCM properties, $Ra_{nl} = \frac{g\beta_{nl}H^3(T_h - T_m)}{\nu_{nl}\alpha_{nl}}$

reduction in the efficiency of LHTES systems [9]. Different approaches for enhancing the thermal conductivity of a PCM have been suggested by researchers, which can be categorized into two main groups. The first group is a geometric approach that is related to a modification in the design of the shape of the enclosure or inserting highly conductive fixed materials such as metal fins and porous materials inside the enclosure [10]. The second approach is based on combining PCM with highly conductive nanoparticles (e.g. copper oxide and aluminum oxide particles) to increase the thermal conductivity of the PCM [11–13]. Although using the reported methods can enhance the thermal conductivity of a PCM, some challenges are remained. For instance, by adding high volume/weight fraction of nanoparticles to a PCM, sedimentation occurs, which has a negative effect on the thermal conductivity of nano-PCM after several cycles of operation [14]. On the other hand, inserting conductive materials (e.g. metal fin, porous material) into the PCM reduces the volume of filled PCM. Because of the lower amount of PCM, lower amount of stored energy will be achieved [15,16]. Different types of geometrical configurations including rectangular, spherical, cylindrical, and annular containers have been studied as a TES system. These are necessitated by the different applications and limitations of the occupied space. A complete description of TES systems with different geometries filled with nano-PCMs can be found in [5,6]. Cylindrical containers can be used both horizontally and vertically, which have invoked a significant interest due to the ease of its manufacturing process. Studying vertical cylindrical containers filled with PCM/nano-PCM, which is the primary focus of the present paper, have been investigated by several researchers. A brief review of studying vertical cylindrical containers filled with PCM/nano-PCM is shown in Table 1.

There are other recently published works regarding the use of nanoparticles to enhance the thermal performance of a LHTES system. For instance, the volumetric heat generation effect during melting/solidification process of nano-PCM filled horizontal cylindrical geometries were studied by Bechiri and Mansouri [27]. Several researchers also investigated the thermal performance of a shell and tube LHTES system filled with nano-PCM [28–33]. In general, it is reported that dispersing nanoparticles at low volume fractions increases the heat transfer rate and because of that the time required for melting/solidification process is decreased. Nonetheless, Parsazadeh and Duan [33] have stated that dispersion of nanoparticles into the PCM increases the melting time due to the degradation of natural convection caused by the addition of Al<sub>2</sub>O<sub>3</sub> into the paraffin wax. The recent investigations regarding the use of nano-PCM in a rectangular LHTES system revealed that dispersion of

highly conductive nanoparticles into the PCM enhances the thermal conductivity of the PCM [34–37]. However, it is mentioned that addition of nanoparticles to the PCM increases the viscosity of PCM, which leads to a decrease in the natural convection that could lower the thermal performance of the LHTES system [35,36]. In addition, nano-PCMs have been also used for several thermal management applications [38–41]. In general, it is concluded that dispersion of nanoparticles at low volume/weight fractions can enhance the amount of removed heat, which can enhance the performance of thermal systems.

According to the published works available in the literature, the melting process of a nano-PCM filled in a vertical C-TES system, which is isothermally heated from its lateral walls and the top and insulated from the bottom, has not been extensively investigated. In the present paper, a numerical investigation on melting process of a bio-based PCM (coconut oil) enhanced with copper oxide (CuO) nanoparticles is performed. Effect of using different volume fractions ( $\phi$ ) of nanoparticles (i.e.  $\phi = 0\%$ ,  $3\%$ ,  $5\%$ ), different cylinder heights of filled nano-PCM representing different Rayleigh ( $Ra$ ) numbers (i.e.  $Ra_{nl} = 10^6$ ,  $10^7$ , and  $10^8$ ) on the melting rate, heat and energy transfer characteristics are studied. Moreover, the behavior of solid-liquid interface at different time intervals is studied.

In the authors' opinion, the authors are the first who have studied the melting process of an edible coconut oil PCM with CuO nanoparticles inside a cylindrical enclosure with isothermal surrounding and adiabatic bottom walls. The relatively inexpensive coconut oil PCM is edible, having the melting temperature ( $\approx 24$  °C) close to the typical lab temperature (22 to 23 °C), and exhibits excellent stability and very small sedimentation for longer uses once nanoparticles are incorporated compared to many other commercially available PCMs reported in the literature. Properties of the nano-PCM were measured and compared with the modeled equation, a maximum discrepancy of  $\pm 5\%$  was observed for the thermal conductivity of nano-PCM. Comprehensive numerical simulation is performed to visualize the progression of the melting process with the experimental comparison; and to calculate the melt fraction, Nusselt number, and energy storage rate.

## 2. Modeling and analysis

A schematic diagram of the vertical C-TES system is presented in Fig. 1. A numerical investigation of the melting process of a bio-based PCM (melting temperature  $T_m$ ) enhanced with different volume fractions of nanoparticles (i.e.  $0\%$ ,  $3\%$ , and  $5\%$  of copper oxide nanoparticles) inside the C-TES system is performed in this work based on

**Table 1**  
Summary of studies on the melting process of PCM/nano-PCM in a vertical cylindrical enclosure.

Authors	Type of study	Melting condition	PCM/nano-PCM	Highlighted findings
Sparrow and Broadbent [17]	Experimental and Numerical	Isothermal heating from the sides, insulated from the bottom	Eicosane as the PCM	<ul style="list-style-type: none"> <li>Fluid motion has a significant effect on the rate of melting and heat transfer</li> <li>Experimental results showed a 50% more transfer of energy compared to numerical results</li> </ul>
Wenzhen et al. [18]	Analytical	Isothermal heating from the sides and the bottom	Eicosane as the PCM	<ul style="list-style-type: none"> <li>Initial sub-cooling of PCM significantly decreased the melting rate</li> <li>An insignificant effect of heat conduction is observed on the melting rate in the liquid phase</li> </ul>
Wu and Lacroix [19]	Numerical	Isothermal heating from the sides, top, and the bottom	Depends on the Prandtl number	<ul style="list-style-type: none"> <li>Increasing the Stefan number led to an increase in the melting rate</li> <li>The bottom surface had the highest rate of heat transfer</li> <li>Conduction was dominated at the top</li> <li>For the case heated from the walls, Benard convection occurred earlier than the case heated only from the bottom</li> </ul>
Jones et al. [20]	Experimental and Numerical	Isothermal heating from the sides, constant temperature at the bottom and insulated from the top	Eicosane as the PCM	<ul style="list-style-type: none"> <li>Four melting regimes including pure conduction, mixed conduction and convection, convection dominant, and shrinking solid occurred during melting process were observed</li> <li>Good agreement between numerical and experimental results were observed for Stefan numbers up to 0.1807</li> </ul>
Shmueli et al. [21]	Numerical with comparison with previous experimental work	Isothermal heating from the sides, insulated from the bottom	RT-27 as the PCM	<ul style="list-style-type: none"> <li>The effect of the mushy zone parameter (C) on the melting process was studied, and it was found that <math>C = 10^6</math> for this parameter had good agreement with experimental work</li> <li>At the beginning of melting process, conduction was the dominant form where with ongoing heating process natural convection dominated. This changed the solid shape to conical shape</li> <li>Adding nanoparticles to the PCM enhanced the thermal conductivity of the PCM</li> </ul>
Wu et al. [22]	Numerical	Heating from the bottom	Copper nanoparticles in Paraffin as the nano-PCM	<ul style="list-style-type: none"> <li>Using 1 wt% of the nano-PCM enhanced melting time up to 13.1%</li> <li>An improvement in melting rate caused by adding nanoparticles was reported</li> <li>A 4% volume fraction of nanoparticles in PCM leads to a 15% decrease in charging time</li> </ul>
Sciacovelli et al. [23]	Numerical	Isothermal heating by using an inner tube at the center of a shell and tube TES system	Copper nanoparticles in Paraffin as the nano-PCM	<ul style="list-style-type: none"> <li>Melting rate was degraded due to decrease of natural convection in the melting process because of increasing viscosity by adding carbon nanotubes</li> </ul>
Zeng et al. [10]	Experimental	Heated from the bottom and insulated from the lateral walls	Carbon nanotubes dispersed in 1-dodecanol as the nano-PCM	<ul style="list-style-type: none"> <li>With a 3 wt% of nanoparticles at the boundary temperature of 55 °C, there was a 8% improve in melting rate</li> <li>Due to the suppression of natural convection by increasing the temperature of boundary condition, the melting rate was degraded</li> <li>A significant increase in the heat transfer rate was reported by using carbon nanotubes and carbon foam</li> </ul>
Fan et al. [24]	Experimental	Isothermally heated from the bottom	Graphene nanoplatelets dispersed in 1-tetradecanol as the nano-PCM	<ul style="list-style-type: none"> <li>A 15% and 25% decrease in the melting time were observed by using 1% volume fraction of single-walled carbon nanotubes (SWCNT) and graphene nanoplatelets (GnP) respectively</li> </ul>
Alshaer et al. [25]	Experimental	Isoflux heating from the bottom	Multi wall carbon nano tubes placed in RT-65 as the nano-PCM and carbon foam as the porous material	<ul style="list-style-type: none"> <li>A 1.5% increase in the melting rate was observed by inclusion of 1% volume fraction of nano-diamond</li> </ul>
Das et al. [26]	Numerical	Isothermal heating by using inner tube inside the shell and tube TES system	n-eicosane and carbon allotropes as the nano-PCM	

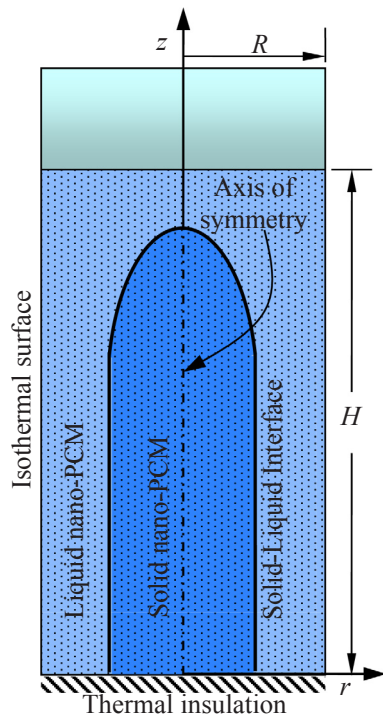


Fig. 1. Schematic diagram of the problem under consideration with dimensions.

the enthalpy-porosity technique. The vertical C-TES system is assumed to have inner diameter ( $d = 2R$ ) of 4.44 cm and is filled with a nano-PCM at different heights ( $H$ ). The C-TES system is isothermally heated from its lateral walls and the top, and insulated from the bottom. The initial temperature ( $T_0$ ) of the system is assumed to be 23 °C, while the lateral wall temperature ( $T_h$ ) is 34 °C. It is worth mentioning that the physical expansion of the PCM during the phase change process was not considered in this work. For the temperature range considered in this paper, the volume expansion of the coconut oil was observed to be small (i.e. approximately 3% for a 20 °C temperature difference) in our experimental work as opposed to many other commercially available PCMs (e.g., Rubitherm, n-octadecane, etc.) reported in the literature. For example, our experiments showed that Rubitherm 22 (RT-22) PCM shows almost 10 to 12% expansion during melting which has melting temperature ( $\sim 22$  °C), close to the melting temperature of coconut oil ( $\sim 24$  °C).

### 2.1. Properties of PCM and nanoparticles

The properties of the copper oxide nanoparticles and the coconut oil used as the PCM are presented in Table 2. The food grade PCM used in this work (i.e., coconut oil) is obtained from a local supplier. For the comparison purpose, the price of the obtained coconut oil and some widely used paraffin based and organic PCMs are provided as follows: (i) coconut oil:  $\sim \$8.0/\text{kg}$  (from DESI), (ii) n-octadecane:  $\sim \$144/\text{kg}$  (from VWR), (iii) Lauric Acid:  $\sim \$89.0/\text{kg}$  (from VWR), and (iv) RT-25:  $\sim \$13.97/\text{kg}$  (from Rubitherm). However, the local supplier could not provide any information on thermophysical properties other than the melting temperature information only. Therefore, the thermophysical properties of PCM (i.e., coconut oil) and nano-PCM (CuO nanoparticles dispersed in coconut oil PCM) were directly measured in our facilities at the University (Advanced Energy Conversion and Control Lab, Bio-Innovation Research Lab, and Food Research Lab). Properties are measured for a temperature range from 10 to 40 °C and for the volume fractions of nanoparticles from 0 to 3.5%.

Thermal conductivity measurements for PCM and nano-PCM were

performed using KD2 Pro handheld device and TPS-500 system. The measured conductivities were identified within the  $\pm 5\%$  error limit with the modeled equations presented in Eqs. (8) and (9). Dynamic viscosity measurements for PCM and nano-PCM were performed using a Rotational Viscometer and a Vibration Viscometer. The measured viscosities were identified within the  $\pm 2.5\%$  error limit with the modeled equation presented in Eq. (7). Density measurements for PCM and nano-PCM were performed using a DMA 35 Density meter. The measured densities were identified within the  $\pm 1.0\%$  error limit with the modeled equation presented in Eq. (5) and (6). Specific heat and heat of fusion measurements for PCM and nano-PCM were performed using a Differential Scanning Calorimeter (DSC). The measured densities were identified within the  $\pm 1.0\%$  error limit with the modeled equation presented in Eqs. (12) and (13).

### 2.2. Approximations and modeled equations

In the current numerical model, the molten or the liquid form of nano-PCM is assumed to be a Newtonian incompressible fluid, and laminar flow is considered for liquid phase bio-based nano-PCM. The density term in the liquid phase of nano-PCM varies linearly with the variation in the temperature, the Boussinesq approximation is adopted in this model. In addition, it is assumed that between the PCM and nanoparticles, the local thermal equilibrium exists. To simplify the problem, a 2-D axisymmetric model is developed. As the melting process starts, thermal energy will flow from the lateral sides of the enclosure to the bio-based nano-PCM. As time advances, the liquid-solid interface can be seen. The principal differential equations, which govern the melting process, are listed below [44]:

$$\text{Mass conservation equation: } \frac{\partial u}{\partial r} + \frac{u}{r} + \frac{\partial w}{\partial z} = 0 \quad (1)$$

where  $u$  and  $w$  are the components of velocity in the radial and axial directions, respectively.

$$\text{Energy conservation equation: } \frac{\partial T}{\partial t} + u \frac{\partial T}{\partial r} + w \frac{\partial T}{\partial z} = \frac{k}{\rho C_p} \left[ \frac{1}{r} \frac{\partial}{\partial r} \left( r \frac{\partial T}{\partial r} \right) + \frac{\partial^2 T}{\partial z^2} \right] \quad (2)$$

where  $T$ ,  $t$ ,  $k$ ,  $\rho$ , and  $C_p$  represent temperature, time, thermal conductivity, density, and specific heat at constant pressure, respectively.

Momentum conservation equation (radial direction):

$$\rho \left( \frac{\partial u}{\partial t} + u \frac{\partial u}{\partial r} + w \frac{\partial u}{\partial z} \right) = -\frac{\partial p}{\partial r} + \mu \left( \frac{\partial^2 u}{\partial r^2} + \frac{1}{r} \frac{\partial u}{\partial r} - \frac{u}{r^2} + \frac{\partial^2 u}{\partial z^2} \right) + A_m \frac{(1-f)^2}{f^3 + \varepsilon} u \quad (3)$$

Momentum conservation equation (axial direction):

Table 2

Thermophysical properties of copper oxide nanoparticles [42,43] and coconut oil.

Thermo-physical properties	Coconut oil		Copper Oxide nanoparticle
	Liquid	Solid	
$\beta$ (1/K) - Coefficient of Thermal Expansion	$7 \times 10^{-4}$	-	$85 \times 10^{-7}$
$h$ (kJ/kg) - Latent heat of fusion	103	-	-
$k$ (W/m K) - Thermal conductivity	0.166	0.228	18
$\mu$ (Pa.s) - Viscosity	0.0268	-	-
$c_p$ (kJ/kg K) - Specific heat	1.67	3.75	0.54
$\rho$ (kg/m <sup>3</sup> ) - Density	918	920	6500
$T_m$ (°C) - Melting Temperature	24	-	-

$$\frac{\partial w}{\partial t} + u \frac{\partial w}{\partial r} + w \frac{\partial w}{\partial z} = -\frac{1}{\rho} \frac{\partial p}{\partial z} + \frac{\mu}{\rho} \left( \frac{\partial^2 w}{\partial r^2} + \frac{1}{r} \frac{\partial w}{\partial r} + \frac{\partial^2 w}{\partial z^2} \right) + g\beta(T - T_m) + A_m \frac{(1-f)^2}{f^3 + \varepsilon} w \tag{4}$$

where  $\mu$ ,  $g$ ,  $\beta$ , and  $T_m$  represent viscosity, gravitational acceleration, coefficient of thermal expansion, and the melting temperature, respectively. The last terms on the right hand side of the momentum equations (i.e., Eqs. (3) and (4)) represent momentum sink, which is described further in Section 2.4.

### 2.3. Thermophysical property relationships

The differences in the amount of the nanoparticles will affect the thermophysical properties of the nano-PCM in different extents. There are several models reported and extensively utilized in the current literature for modeling and calculating thermophysical properties (i.e., conductivity, viscosity, etc.) of nano-fluids and nano-PCMs. The thermophysical property relationships as given in Eqs. (5)–(13) below [45,46,9,47] are approximately suitable for the nano-PCM used in this paper, where subscripts ‘nl’, ‘ns’, ‘n’, ‘l’, ‘s’ refer to properties of liquid nano-PCM, solid nano-PCM, nanoparticles, liquid PCM, and solid PCM, respectively.

$$\text{Density of nano-PCM, liquid phase: } \rho_{nl} = (1-\phi) \rho_l + \phi \rho_n \tag{5}$$

$$\text{Density of nano-PCM, solid phase: } \rho_{ns} = (1-\phi) \rho_s + \phi \rho_n \tag{6}$$

$$\text{Dynamic viscosity of nano-PCM, liquid phase: } \mu_{nl} = \frac{\mu_l}{(1-\phi)^{2.5}} \tag{7}$$

$$\begin{aligned} &\text{Thermal conductivity of nano-PCM, liquid phase} \\ &: k_{nl} = \frac{k_n + 2k_l - 2\phi(k_l - k_n)}{k_n + 2k_l + \phi(k_l - k_n)} k_l \end{aligned} \tag{8}$$

$$\begin{aligned} &\text{Thermal conductivity of nano-PCM, solid phase} \\ &: k_{ns} = \frac{k_n + 2k_s - 2\phi(k_s - k_n)}{k_n + 2k_s + \phi(k_s - k_n)} k_s \end{aligned} \tag{9}$$

$$\begin{aligned} &\text{Expansion coefficient of nano-PCM, liquid phase} \\ &: (\rho\beta)_{nl} = (1-\phi)(\rho\beta)_l + \phi(\rho\beta)_n \end{aligned} \tag{10}$$

$$\begin{aligned} &\text{Expansion coefficient of nano-PCM, solid phase} \\ &: (\rho\beta)_{ns} = (1-\phi)(\rho\beta)_s + \phi(\rho\beta)_n \end{aligned} \tag{11}$$

$$\begin{aligned} &\text{Heat capacity of nano-PCM, liquid phase} \\ &: (\rho C_p)_{nl} = (1-\phi)(\rho C_p)_l + \phi(\rho C_p)_n \end{aligned} \tag{12}$$

$$\begin{aligned} &\text{Heat capacity of nano-PCM, solid phase: } (\rho C_p)_{ns} = (1-\phi)(\rho C_p)_s + \phi(\rho C_p)_n \end{aligned} \tag{13}$$

As mentioned earlier, thermophysical properties are measured for different values of  $\phi$  (up to 3.5%) and compared to the values obtained from Eqs. (5), (7), (8), and (12), respectively. It is identified that the discrepancies between using the equations and the measured values are within the  $\pm 1\%$  error limit for the density and the specific heat, within the  $\pm 2.5\%$  error limit for the viscosity, and within the  $\pm 5\%$  error limit for the thermal conductivity. Therefore, during the numerical simulations, thermophysical property relationships (i.e., Eqs. (5)–(13)) are used. Additionally, several samples of nano-PCM with different volume fractions were stored in the lab for approximately 30 weeks and periodically tested by melting and solidifying them in a controlled temperature environment. A small amount of sedimentation was observed for the larger  $\phi$  (approximately 2%).

**Table 3**  
Properties of the nano-PCM at the transition stage [9,47,48].

Properties	Range of Temperatures		
	$T < T_m$	$T_m \leq T \leq T_m + \Delta T_m$	$T > T_m + \Delta T_m$
$k$	$k_{ns}$	$\frac{k_{ns} + k_{nl}}{2}$	$k_{nl}$
$\rho$	$\rho_{ns}$	$\frac{\rho_{ns} + \rho_{nl}}{2}$	$\rho_{nl}$
$(\rho C_p)$	$(\rho C_p)_{ns}$	$\frac{(\rho C_p)_{ns} + (\rho C_p)_{nl}}{2} + \frac{\rho_{ns} + \rho_{nl}}{2} \left( \frac{h_{sl,n}}{\Delta T_m} \right)$	$(\rho C_p)_{nl}$
$\mu$	$10^6$	–	$\frac{\mu_l}{(1-\phi)^{2.5}}$

### 2.4. Mushy zone (or transition zone) approximation

It should be noted that the change in phase (i.e., solid to liquid) of the nano-PCM occurs gradually within a transition stage. At this stage, the properties of nano-PCM are influenced by a transition temperature interval (i.e.,  $\Delta T_m$ ) which is observed to be approximately 1 °C for the PCM considered in this work. Table 3 presents the variation in the thermophysical properties of nano-PCM (i.e., density, heat capacity, viscosity, and thermal conductivity) within different temperature ranges with respect to  $T_m$  and  $\Delta T_m$ : where  $h_{sl,n}$  is the latent heat of fusion of nano-PCM and can be calculated by the following equation:

$$h_{sl,n}(1-\theta)h_{sl} \tag{14}$$

At the transition stage, the value of specific heat increases into a higher value compared to the solid and the liquid phase. The increment in the specific heat is caused by the high absorption of heat in form of latent heat within a small temperature range. In addition, in the transition stage, the viscosity drops from a high value in the solid phase to low value in the liquid phase. To handle these changes, mushy zone parameters [49,50] are used. As it is indicated in Eqs. (3) and (4), the mushy zone is modelled using an additional source term (i.e., momentum sink) in the governing momentum equations. In the momentum equations the sink terms are  $A_m \frac{(1-f)^2}{f^3 + \varepsilon} u$  and  $A_m \frac{(1-f)^2}{f^3 + \varepsilon} w$ , where  $A_m$  is the mushy zone parameter ( $= 10^5$ ),  $f$  is the melting region identifier, and  $\varepsilon$  ( $= 10^{-8}$ ) is a small number to avoid division by zero. The identifier is given by  $f = 0$  in the solid region (i.e.,  $T < T_m$ ),  $f = 1$  in the liquid region (i.e.,  $T > T_m + \Delta T_m$ ), and  $0 < f < 1$  (i.e.,  $T_m \leq T \leq T_m + \Delta T_m$ ) [50].

### 2.5. Boundary and initial conditions

The following initial and boundary conditions have been considered:

$$\begin{aligned} &\text{Initial condition } (t = 0): T(r,z,0) = T_0, u = w = 0, \\ &\text{Bottom part of the C- TES system } (t > 0): \frac{\partial T(r,0,t)}{\partial z} = 0, u = w = 0, \\ &\text{Lateral wall of the C- TES system } (t > 0): T(R,z,t) = T_h, u = w = 0, \\ &\text{Upper part of the C- TES system } (t > 0): T(r,H,t) = T_h, u = w = 0. \end{aligned} \tag{15}$$

### 2.6. Energy storage rate

The amount of the stored energy during the melting process can be defined by calculating the energy transferred from hot lateral walls to the cold nano-PCM during the melting process. The transferred energy can be defined as the time integration of the instantaneous heat transfer rate during the melting process, which is presented in equations below [51].

$$E = \int_0^t \dot{Q}(t) dt \tag{16}$$

where  $\dot{Q}(t)$  is the instantaneous heat transferred at the system

boundaries during melting process defined as:

$$\dot{Q}(t) = (\pi d) \int_0^H \left(-k \frac{\partial T}{\partial r}\right)_{r=R} dz + (2\pi) \int_0^R \left(-k \frac{\partial T}{\partial z}\right)_{z=H} r dr \quad (17)$$

where  $d (=2R)$  is the inner diameter of the C-TES system and  $k$  represents the thermal conductivity of the nano-PCM. Further, the heat transfer from the hot lateral wall to the cold nano-PCM can be evaluated by the average Nusselt number, which may be calculated based on either thermal conductivity of PCM,  $k_f$ , or thermal conductivity of the nano-PCM,  $k_{nf}$ . The following equations can be used for calculating the average Nusselt number:

$$\text{Nusselt number based on } k_{nf}: Nu_n = \frac{hH}{k_{nf}} = -\frac{1}{T_h - T_m} \int_0^H \left(\frac{\partial T}{\partial r}\right)_{r=R} dz \quad (18a)$$

$$\begin{aligned} \text{Nusselt number based on } k_f: Nu_f &= \frac{hH}{k_f} \\ &= -\frac{1}{T_h - T_m} \left(\frac{k_{nf}}{k_f}\right) \int_0^H \left(\frac{\partial T}{\partial r}\right)_{r=R} dz \end{aligned} \quad (18b)$$

where  $h$  represents the surface averaged convection heat transfer coefficient. Note however that the magnitudes of  $Nu_n$  and  $Nu_f$  may be different for a given condition, the value of  $h$  will remain same irrespective of these definitions.

2.7. Solution technique, grid and time interval dependency tests, and validation

Eqs. (1)–(4) are numerically solved given the initial and boundary conditions using a 2D axisymmetric model developed by the finite-element based COMSOL Multiphysics® software. Three different mesh sizes including 3471, 8255, and 19,209 elements are used to examine the mesh dependency. The melting fraction (MF) for  $Ra_{nl} = 10^6$  and  $\phi = 3\%$  is numerically calculated by using three different described meshes above and the corresponding result is presented in Fig. 2a and Table 4. The percentage of melting fraction (MF) is calculated using the following equation:

$$MF = \frac{\text{Volume of the liquid nano-PCM}}{\text{Total(solid + liquid)volume of the nano-PCM}} \times 100\%. \quad (19)$$

As it can be seen from Fig. 2a and Table 4, a slight difference among the melting fractions are observed towards the end of the melting process.

Therefore, to ensure the accuracy of the results and reduce the simulation time, the mesh size with 8255 is adopted for further calculations. A magnified view of the considered mesh is presented in Fig. 2b. As it can be seen, a non-uniform distribution of mesh with higher concentration of elements near the rigid walls of the C-TES system is considered. In addition, the detailed information regarding the elements used in this mesh is shown in Table 5.

In the next step, the time dependency test is examined. To do so, the melting fraction for the similar case as the above are numerically calculated using three different time intervals as shown in Table 6. The results of this test are shown in Fig. 2c and Table 7.

As it can be observed from Table 7 and Fig. 2c, the melting fraction values at three different selected values are almost identical for the mentioned time intervals. As a result, the time independency of the numerical model is concluded.

To validate the accuracy of the current numerical model, simulations are carried out to reproduce some results from Shmueli et al. [21]. Shmueli et al. [21] performed a numerical investigation to study the melting process of RT-27 filled in vertical cylindrical tubes. Shmueli et al. [21] considered two different cylindrical tubes with the diameters of 3 cm and 4 cm and height of 17 cm. These cylinders were insulated from the bottom and heated isothermally from their sides. The initial

temperature of the RT-27 was set to 22 °C and was heated 10 °C and 30 °C above the melting temperature of RT-27. To check the accuracy of the present work, similar conditions as described in Shmueli’s [21] work were set. The thermophysical properties of RT-27 are shown in Table 8.

A comparison is presented in Figs. 3 where numerically obtained images representing different melting stages are compared for four selected times (i.e., 8 min., 20 min., 32 min., and 36 min.). In each image, the solid PCM, liquid PCM, and solid-liquid interface are clearly visible. Additionally, experimentally obtained images, reported in Shmueli et al. [21] are added in Fig. 3a and comparisons are explained below.

- (i) Images at 8 min. (Fig. 3a(i)): Images from present and Shmueli et al.’s [21] numerical works are almost identical with a thin layer of liquid PCM close to the vertical wall. The thickness of the liquid layer in the experimental work seems slightly larger than both numerical works. The top part of the solid PCM is slightly curved for both numerical works, which is similar to the experimental image.
- (ii) Images at 20 min. (Fig. 3a(ii)): Portion of the upper part of the enclosure occupied by the liquid PCM is bigger in size in the present numerical image than the Shmueli et al.’s [21] numerical image. However, the experimental image shows a size that lies in between two numerical works. The curvature of the top solid PCM from present simulation work is similar to that of Shmueli et al.’s [21] experimental work.
- (iii) Images at 32 min. (Fig. 3a(iii)): Portion of the upper part of the enclosure occupied by the liquid PCM is bigger in size in the present numerical image than the Shmueli et al.’s [21] numerical image. However, the vertical liquid layer in Shmueli et al.’s [21] work is relatively thicker in size than the present numerical work. Shmueli et al.’s [21] experimental image shows a size that lies in between two numerical works. The curvature of the top solid PCM for all cases shows an inverted dome pattern.
- (iv) Images at 36 min. (Fig. 3a(iv)): Most discrepancy between present numerical and Shmueli et al.’s [21] numerical works is observed here. However, the height of the solid PCM for present numerical work is close to the Shmueli et al.’s [21] experimental work.

In summary, it can be argued that a fair agreement is obtained

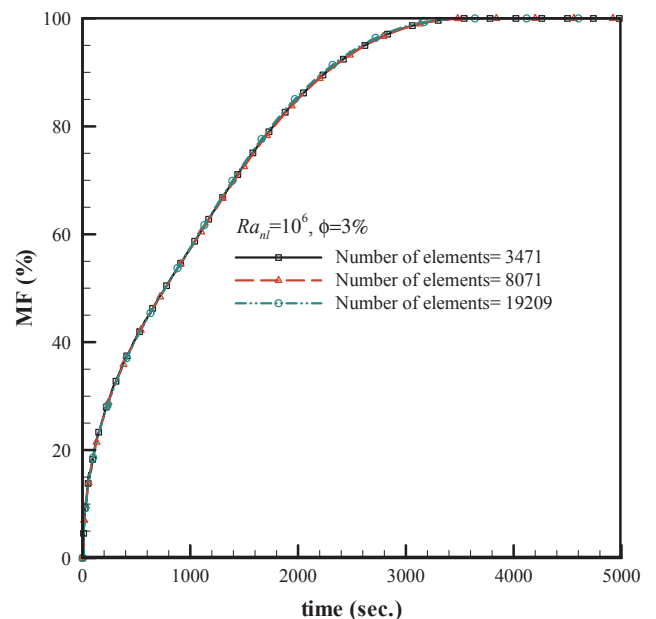


Fig. 2a. Melting fraction for three different mesh qualities ( $Ra_{nl} = 10^6$ ,  $\phi = 3\%$ ).

**Table 4**  
Melting fraction values for three different mesh qualities at three selected times,  $Ra_{nl} = 10^6$ , and  $\phi = 3\%$ .

No. of elements	MF at 1000 s	MF at 2000 s	MF at 3000 s
3471	57.29%	85.04%	98.26%
8255	57.38%	85.17%	98.30%
19,209	57.54%	85.66%	98.52%

between the present work and numerical/experimental works reported by Shmueli et al. [21]. Additional comparisons are reported in Section 3.4.

In addition to the qualitative comparison presented above, a quantitative comparison is presented in Fig. 3b where results obtained from current simulation using the case of Shmueli et al.'s [21] are compared with the experimental and numerical work reported in [21]. As can be observed, the current simulation has a very good agreement with Shmueli et al.'s [21] numerical work. However, their experimental work shows more discrepancy beyond 2000 s. It can be further observed from Fig. 3b that the difference between the experimentally and numerically obtained melt fractions obtained from Shmueli et al. [21] is beyond 5% error limit after 2000 s (MF > 78%). Therefore, our validation decision is based on the agreement between numerically obtained melt fraction values from current simulation and numerically obtained melt fraction values reported in Shmueli et al. [21].

### 3. Results and discussion

Results obtained from numerical simulations are presented and discussed in this section. Results include images during the melting process, percentage of melting fraction, Nusselt number, and rate of energy storage. These parameters are presented for different values of nanoparticles volume fraction and Rayleigh number. In this study, Rayleigh number is corresponded to laminar flow and can be defined

**Table 5**  
Details of the mesh elements for  $Ra_{nl} = 10^6$ .

Name of the elements	Number of elements
Triangular	7348
Quadrilateral	556
Edge	342
Vertex	9

**Table 6**  
Time intervals used to examine the time dependency.

Starting time (s)	Ending time (s)	Time step (s)		
			Present simulation	Test 1
0	10	0.01	0.1	0.005
10	100	0.1	1	0.05
100	10,000	10	100	5

either based on the liquid nano-PCM properties ( $Ra_{nl}$ ) or liquid base-PCM properties ( $Ra_l$ ) as shown in Eqs. (20a) and (20b) below:

Rayleigh number based on liquid nano-PCM properties

$$: Ra_{nl} = \frac{g\beta_{nl}H^3(T_h - T_m)}{\nu_{nl}\alpha_{nl}} \tag{20a}$$

Rayleigh number based on liquid base-PCM properties

$$: Ra_l = \frac{g\beta_l H^3(T_h - T_m)}{\nu_l \alpha_l} \tag{20b}$$

It should be noted that the magnitude of  $Ra_{nl}$  changes with changing  $\phi$  as thermophysical properties of liquid nano-PCM (i.e.,  $\mu_{nl}$ ,  $\alpha_{nl}$ ,  $\beta_{nl}$ , etc.) depend strictly on  $\phi$ . Therefore, to keep  $Ra_{nl}$  constant with changing  $\phi$  the magnitude of  $H$  should be adjusted for a given reference

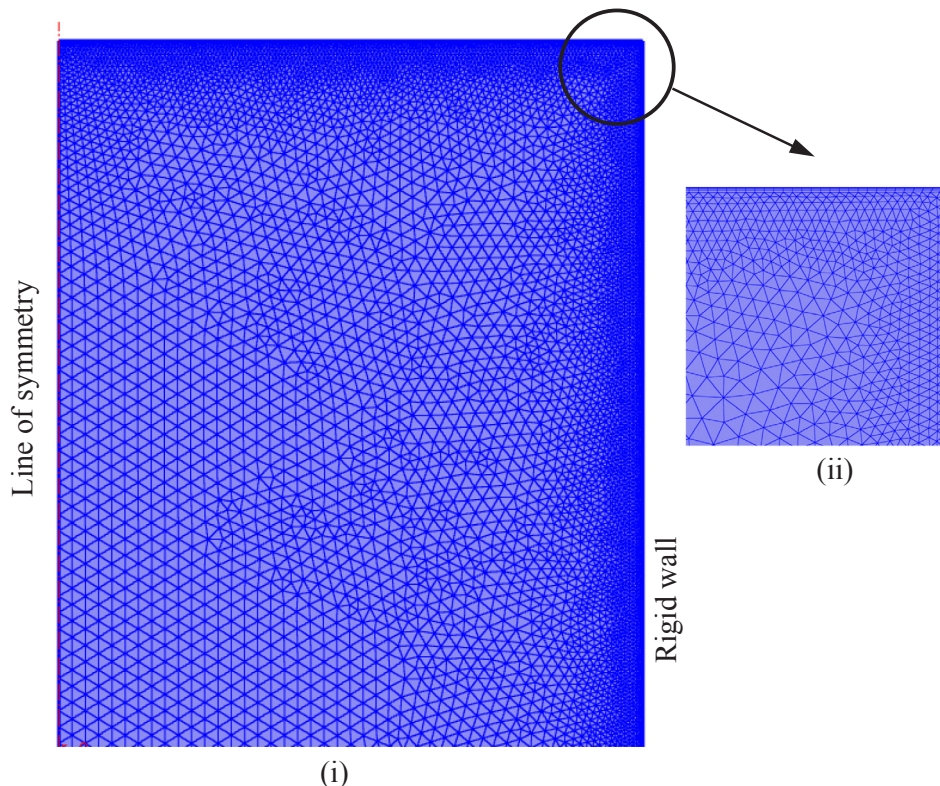


**Fig. 2b.** (i) A magnified view of the mesh distribution inside the C-TES system and (ii) a magnified view of the mesh distribution at the upper left corner of the geometry.

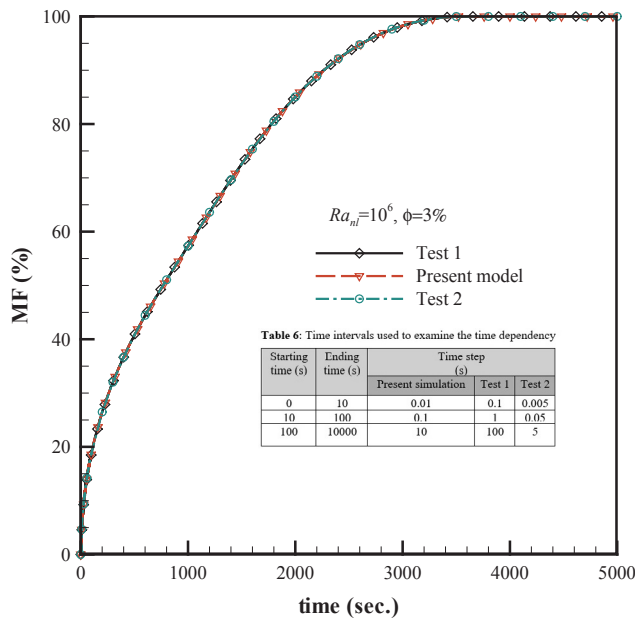


Fig. 2c. Melting fraction calculated with three different time intervals ( $Ra_{nl} = 10^6$ ,  $\phi = 3\%$ ).

Table 6: Time intervals used to examine the time dependency

Starting time (s)	Ending time (s)	Time step (s)		
		Present simulation	Test 1	Test 2
0	10	0.01	0.1	0.005
10	100	0.1	1	0.05
100	10000	10	100	5

Table 7: Melting fraction values for three different time intervals ( $Ra_{nl} = 10^6$ ,  $\phi = 3\%$ ).

Model	MF at 1000 s	MF at 2000 s	MF at 3000 s
Present simulation	57.29%	85.04%	98.26%
Test 1	57.31%	85.04%	98.3%
Test 2	57.32%	85.03%	98.26%

Table 8: Thermophysical properties of RT-27 [52].

Thermo-physical properties	Rubitherm, RT-27	
	Liquid	Solid
$\beta$ (1/K) - Coefficient of Thermal Expansion	0.0005	–
$h$ (kJ/kg) - Latent heat of fusion	179	–
$k$ (W/m K) - Thermal conductivity	0.15	0.24
$\nu$ (m <sup>2</sup> /s) - Kinematics Viscosity	$3.42 \times 10^{-3}$	–
$c_p$ (J/kg K) - Specific heat	1800	2400
$\rho$ (kg/m <sup>3</sup> ) - Density	760	870
$T_m$ (°C) - Melting Temperature	28–30	

temperature difference (i.e.,  $T_h - T_m$ ). However,  $Ra_l$  does not change with any changes in  $\phi$  as the thermophysical properties of base-PCM (i.e.,  $\mu_l$ ,  $\alpha_l$ ,  $\beta_l$ , etc.) are independent of  $\phi$ . Both  $Ra_{nl}$  and  $Ra_l$  are extensively used in the literature related to nanofluids and nano-PCMs. In this paper,  $Ra_{nl}$  is used to include the effect of adding nanoparticles with different  $\phi$ .  $Ra_{nl}$  gives some advantages over  $Ra_l$  while establishing correlation with other dimensionless parameters, such as, Nusselt number.

### 3.1. Evolution of solid-liquid interface and trend of melting fraction

Fig. 4 shows the evolution of solid-liquid interface of nano-PCM inside the C-TES system at  $Ra_{nl} = 10^6$  for three selected volume fractions of nanoparticles (i.e.  $\phi = 0\%$ ,  $3\%$ , and  $5\%$ ). For each  $\phi$ , numerically obtained thermal images are presented at six selected times to cover a range of characteristic melting regimes. Corresponding values of melting fractions are presented in the individual figure title as well. Note that the height of the enclosure has to be adjusted slightly to keep  $Ra_{nl} = 10^6$  at  $\phi = 3\%$  (5.1% increase in height compared to  $\phi = 0\%$

case) and  $5\%$  (8.7% increase in height compared to  $\phi = 0\%$  case). Each row in Fig. 4 implies the effect of melting time, while each column implies the effect of  $\phi$ . At the beginning of the melting process, the entire nano-PCM is in the solid form at the initial temperature ( $T_0$ ). Just after initiation of the higher wall temperature ( $T_h$ ), the solid nano-PCM adjacent to heated walls of the C-TES system absorbs the thermal energy from the walls, which increases the solid nano-PCM’s temperature sensibly, until it reaches the melting temperature ( $T_m$ ). At this stage (e.g., see Fig. 4(a)) vertical thin layers of liquid nano-PCM adjacent to lateral walls and at the top are appeared which lead to having a solid-liquid interface. Conduction is the dominant heat transfer mode at early stages of melting process, as the narrowness of the liquid nano-PCM layers allow the dominance of the viscous force over the buoyancy or inertial forces, resulting in a motionless (or nearly motionless) liquid nano-PCM. These layers will grow as heating continues. With ongoing heating, buoyancy or inertial forces overcome the viscous force, which will initiate the upward motion of warm liquid nano-PCM. This motion is pronounced initially at the top corners of the enclosure. Specifically, a relatively wider region of liquid nano-PCM is observed at the upper edges of the enclosure, which grows as time advances further. However, at the lower part of the vertical liquid layers of the nano-PCM, conduction is still the dominant mode of heat transfer (see Fig. 4(b)). This combined natural convection and conduction dominated melting zone can be termed as the mixed or transition regime of melting. As time furthers, natural convection becomes more dominant, thus widening up more space filled with liquid nano-PCM. Thermal stratification and convective motion simultaneously assist accumulation of more thermal energy at the upper part, resulting in a curved interface at the top. As time advances further, intensified convection motion melts down remaining solid nano-PCM gradually. At some stage, conduction dominated melting is completely diminished and this can be attributed from the change in the shape of the remaining solid nano-PCM from a nearly flat pattern to a dome shape pattern (see Fig. 4(c)–(f)). Adding nanoparticle does not show a significant improvement on the melting rate at the early stage of the melting process where conduction heat transfer dominates. Although adding nanoparticles improved the thermal conductivity of the nano-PCM and reduce slightly the thermal resistant in the liquid layers, due to the motionless molten nano-PCM, there is not a significant improvement in the melting rate at these stages. Note however that the size of the enclosure is slightly bigger for  $\phi = 3\%$  and  $\phi = 5\%$ . However, as it can be seen from Fig. 4(f), (l), and (r), adding nanoparticles improved the melting rate at the later stages of the melting process. At these stages, natural convection is the dominant form of heat transfer. By adding nanoparticles with different  $\phi$ , the dominance of natural convection occurs earlier, which results in higher melting fraction rates. Therefore, increasing the  $\phi$  from  $3\%$  to  $5\%$  showed more improvement on the melting rate. Figs. 5a and 5b show the effect of  $Ra_{nl}$  on the progression of melting process at  $\phi = 3\%$ . Note that 2.17 and 4.64 times increase in the  $H$  are required to achieve  $Ra_{nl} = 10^7$  and  $Ra_{nl} = 10^8$ , respectively, from  $Ra_{nl} = 10^6$ . In Fig. 5a, thermal images are selected in a way to match the percentage melting fractions closely at all three  $Ra_{nl}$  s. The corresponding times of melting are presented in the figure as well. An increase in  $Ra_{nl}$  implies an increase in the height of the nano-PCM, which results in larger time of melting to achieve same level of melting fractions at higher  $Ra_{nl}$ . An increase in  $Ra_{nl}$  further implies stronger buoyancy force and this can be attributed to the shape of the remaining solid nano-PCM at higher  $Ra_{nl}$ . For the case of  $Ra_{nl} = 10^6$ , the shape resembles a dome, while at  $Ra_{nl} = 10^8$ , it is like a slender inverted parabola. The distance between dominance of natural convection regime close to the top of the enclosure and the remaining solid nano-PCM increases as well at higher  $Ra_{nl}$  (see images Fig. 5a(j) and (p)). Similar behavior is shown in Fig. 5b where melting progression at the same time intervals is presented.

Fig. 6 presents the trend of melting fraction at different  $\phi$  and  $Ra_{nl}$ . Due to the high temperature difference between hot wall and cold solid nano-PCM at the beginning of the melting process, the melting rate is

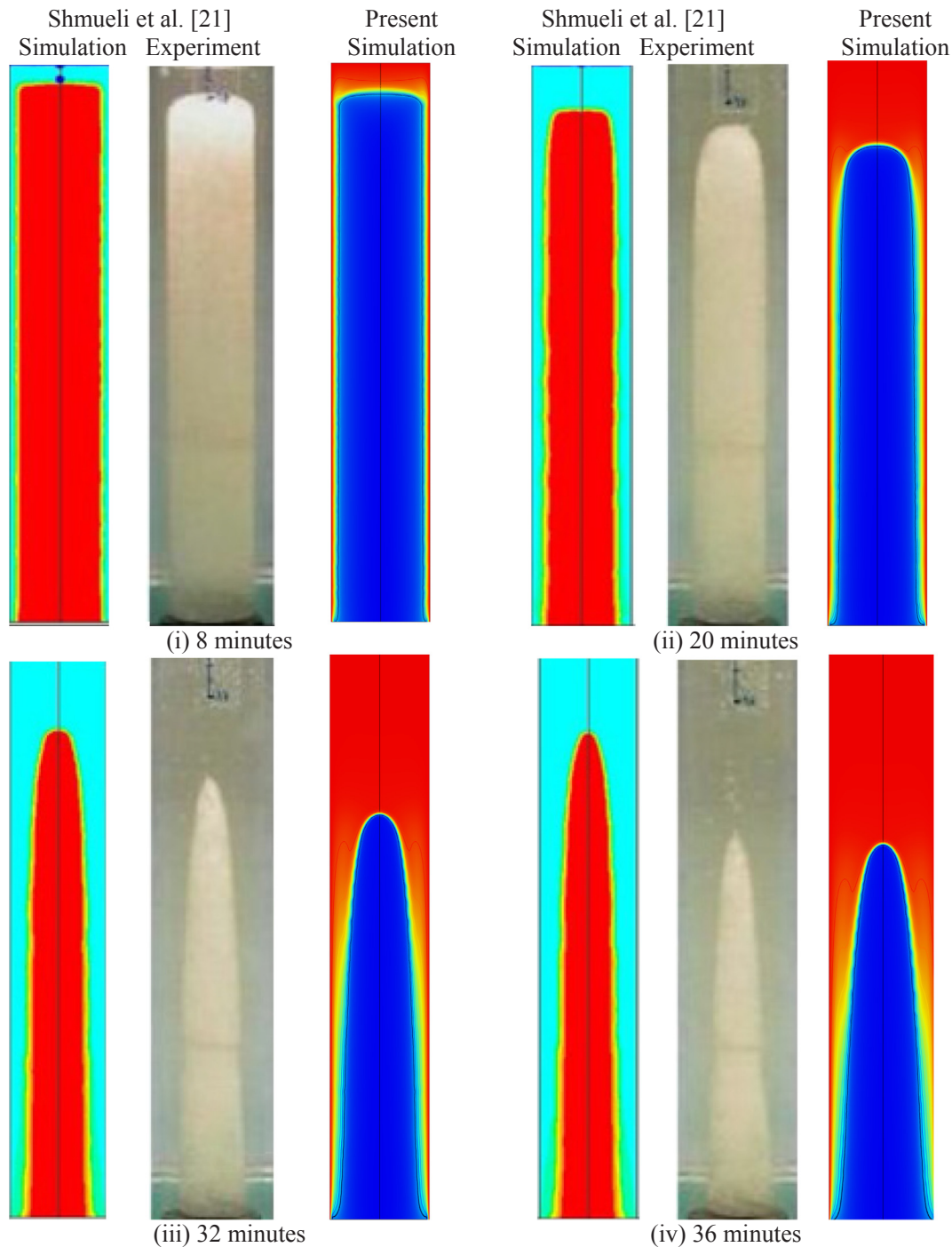


Fig. 3a. Validation of the numerical model with previously published work in the literature [21].

high. Therefore, the slope of the melting fraction curvature at the beginning (e.g., 200 s) is higher than subsequent time intervals. As discussed earlier, dispersing nanoparticles into the PCM at the early stages showed an insignificant impact on the melting rate which can be clearly observed from MF-time plot for all  $\phi$ . For better understanding, a quantitative comparison is presented in Table 9 for time  $t = 300$  s.

Temperature increased faster in the nano-PCM than the pure PCM due to higher thermal conductivity. This resulted in a higher melting rate in nano-PCM than pure PCM. Adding nanoparticles to the PCM reduces the latent heat of fusion of the nano-PCM, which implies that less amount of energy is required for melting as long as the difference between the hot lateral wall temperature and the melting temperature of the nano-PCM remains constant. As a result, higher melting rate is

expected after adding nanoparticles. It is clear from Fig. 6 that the nano-PCM having  $\phi = 5\%$  shows a higher melting rate than nano-PCM with  $\phi = 3\%$ . However, adding higher volume fractions of nanoparticles does not always lead to a proportional increase in the melting rate. The reason behind this statement is that, in general cases (except heavy oils used as the PCM) adding nanoparticles to a PCM, increases the viscosity of the PCM, which will suppress the natural convection during the melting process [10,53]. Although increasing the height of the filled nano-PCM in the C-TES system will increase the heat transfer area, it increases the quantity of the nano-PCM as well, which requires more time to melt. At the last stages of the melting process, the enclosure is occupied by the liquid nano-PCM followed by a small amount of solid nano-PCM at the bottom of the enclosure. The interface area

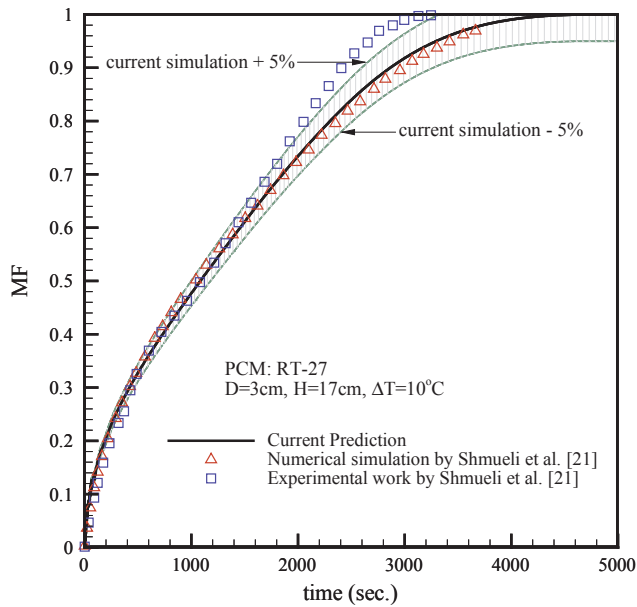


Fig. 3b. Validation of the simulated result with result obtained in Shmueli et al. [21].

between the solid and liquid nano-PCM is relatively small. Therefore, melting process slows down towards the end resulting in a change in the slope of the MF-time curve.

### 3.2. Trend of the surface-averaged $Nu_n$ number

In this section, attention is given to characterize and discuss the surface average heat flux which is presented as dimensionless Nusselt number ( $Nu_n$ ). The transient variation of the surface-averaged  $Nu_n$  throughout the melting process is presented in Fig. 7. The  $Nu_n$ -time profiles in Fig. 7 exhibit a unique pattern variation at different time ranges during melting as opposed to the MF-time profile (see Fig. 6) where MF grows monotonically as time advances. As discussed earlier, the conduction dominates the melting process and creates a thin layer of liquid nano-PCM initially. The thermal resistance inside this thin liquid layer is relatively low, resulting in a relatively high temperature gradient and a high heat flux. Therefore, the magnitude of the  $Nu_n$  is higher at the initial stages of the melting process. This thin liquid layer grows in the conduction dominated regime as time advances. As a result of that a sharp drop in the magnitude of the  $Nu_n$  is observed and this sharp drop is ceased at a particular time (depending on  $Ra_{nl}$ ) with a clear change in the slope of  $Nu_n$ -time profile. The change in slope is an early indication of the formation of thermal boundary layer and the initiation of the convective motion at the upper part of the liquid layer. Heat transfer rate is relatively high inside this growing boundary layer region, while it is still the opposite inside the diminishing conduction dominated regime. Therefore, the two opposing trends in heat transfer inside the mixed convection and conduction regime (i.e., the transition regime) causes the slope change in  $Nu_n$ -time profile. As discussed in Bejan [26], Nusselt number remains constant (i.e., independent of time variation, but function of Rayleigh number) inside a fully convection dominated melting regime where height of the remaining solid PCM remains equal to the enclosure height until a particular time. A true

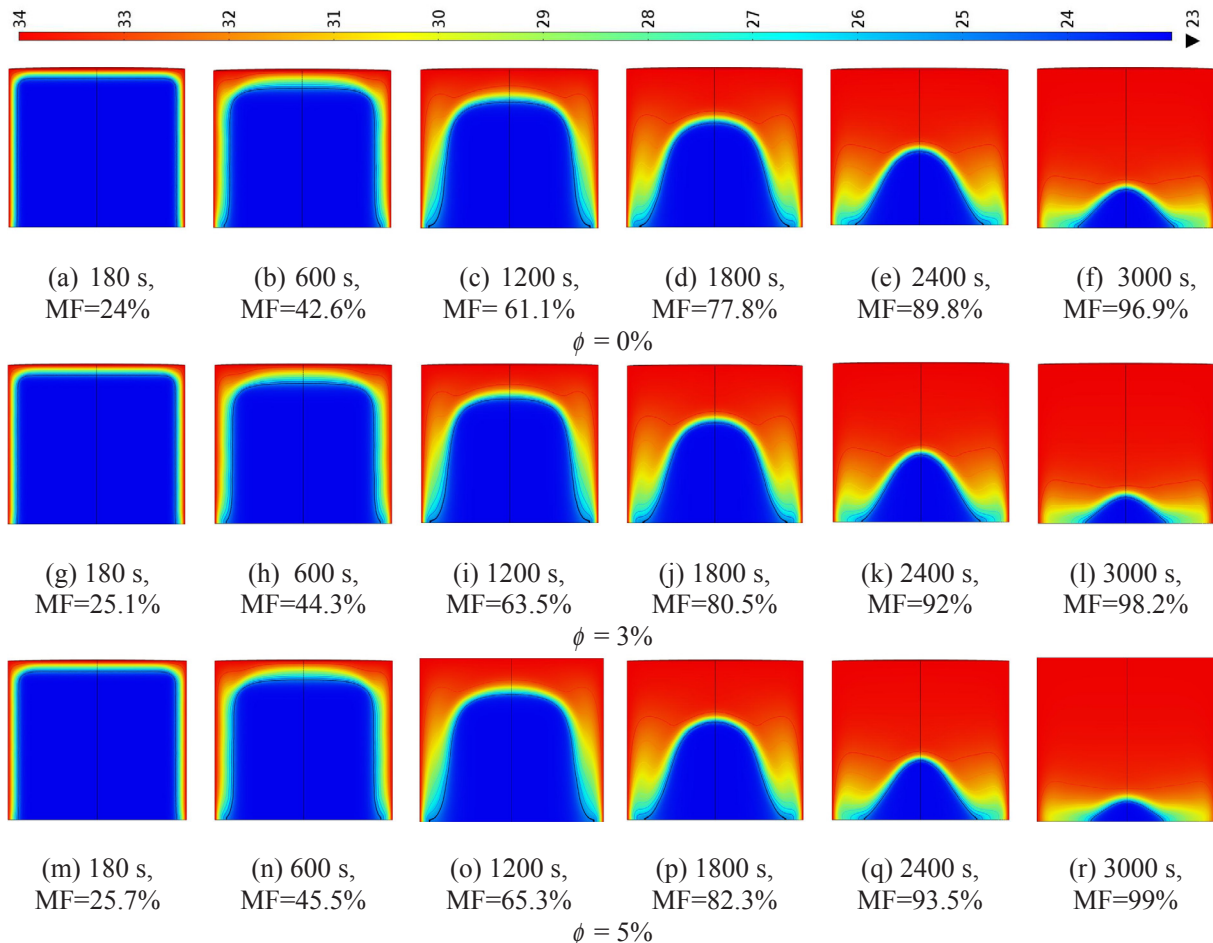


Fig. 4. Effect of different volume fractions of nanoparticle on the melting progression at different time for  $Ra_{nl} = 10^6$ .

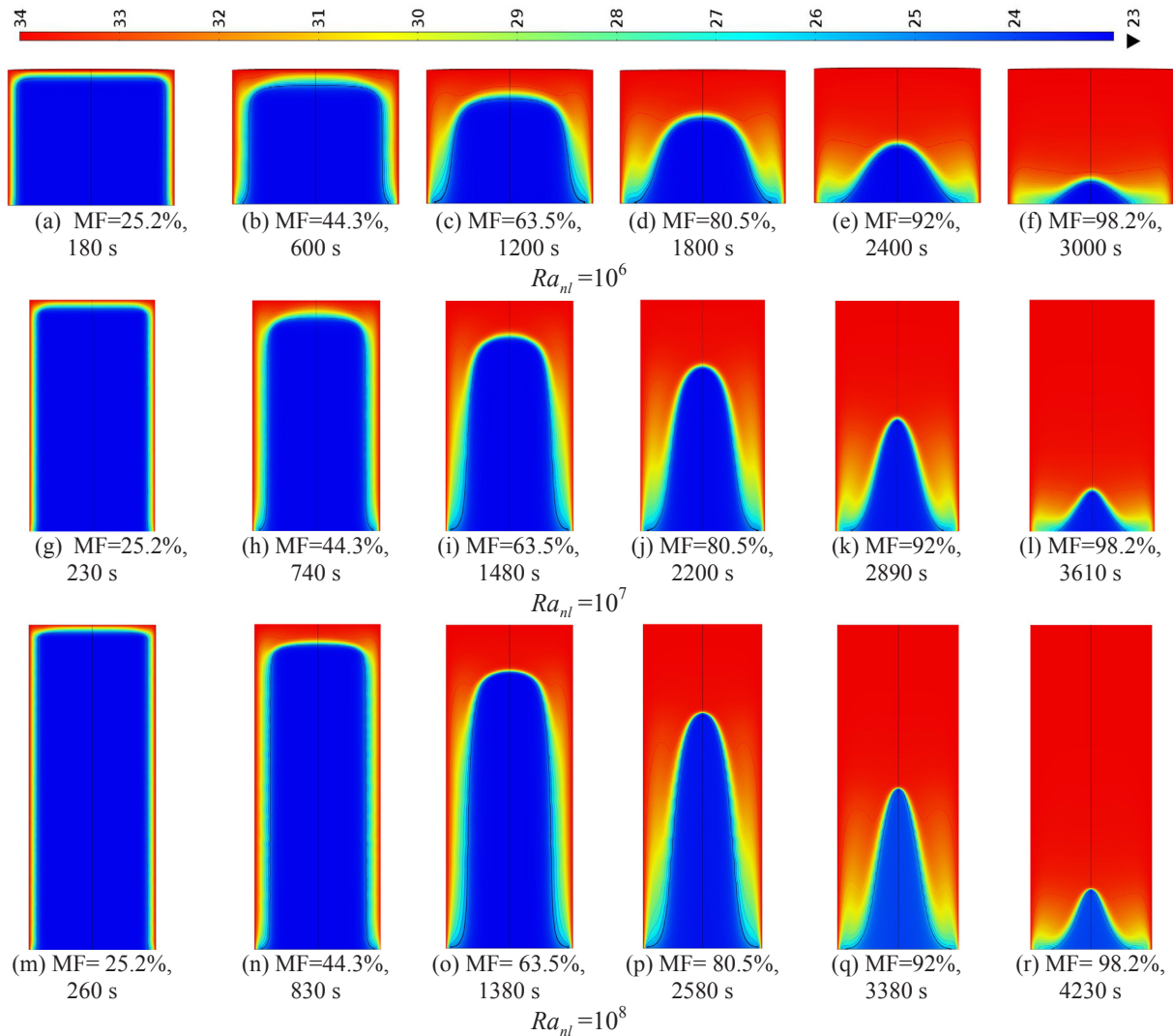


Fig. 5a. Effect of different  $Ra_{nl}$  on the melting progression at different time for a given  $\phi = 3\%$  and the same MF.

fully convection dominated regime does not exist in the current study; instead convection dominated melting occurs in parallel with the shrinking solid nano-PCM. Therefore, just after the conduction regime diminishes completely, another change in the slope is observed in the  $Nu_n$ -time profile. Throughout the combined convection dominated and shrinking solid nano-PCM regime,  $Nu_n$  drops as time advances. At the end of the melting process, where nano-PCM is melted completely, the liquid nano-PCM reaches a thermal equilibrium with the wall temperature while ceasing any heat transfer through the wall,  $Nu_n$  drops to a minimum value with final change in the slope of  $Nu_n$ -time profile.

In the conduction dominated regime,  $Nu_n$  variations with time is nearly unaffected by any change in  $\phi$ . Note that, in the pure conduction dominated melting zone,  $Nu_n$  is proportional to the ratio of wall heat flux to the thermal conductivity of the nano-PCM. As discussed earlier, both wall heat flux and thermal conductivity increase with increasing  $\phi$  in the conduction regime,  $Nu_n$  remains nearly unchanged with changing  $\phi$  in this regime. Gradual variation in the magnitude of  $Nu_n$  with changing  $\phi$  is observed in the transition and subsequent regimes of melting. It is observed that adding nanoparticles into the PCM decrease the magnitude of the  $Nu_n$  where a larger reduction in the magnitude is observed for greater  $\phi$ , specifically, toward later stages of combined convection and shrinking solid regimes. Note however that a reduction in  $Nu_n$  does not always imply a reduction in the heat transfer rate. To assist this concern further, the behavior of the convective heat transfer

coefficient ( $h$ ) at different  $\phi$  is plotted within Fig. 7. A higher value of  $h$  is observed at larger  $\phi$ . As  $Nu_n$  is proportional to  $h/k_{nf}$ , a reduction in  $Nu_n$  in this case refers to a smaller  $h/k_{nf}$  at higher  $\phi$ . Nano-PCM properties are affected by any change in the volume fraction of nanoparticles; more elaborately, an increase in the value of  $\phi$  increases the thermal conductivity and the density, but decreases the specific heat and heat of fusion of the PCM. Due to such change in the property values, it is observed that the value of the Rayleigh number decreases with increasing  $\phi$  if the height of the enclosure is fixed. Therefore, the height of the enclosure is adjusted each time to keep  $Ra_{nl}$  constant with changing  $\phi$ . For example, consider the case of  $Ra_{nl} = 10^8$  in Fig. 7, the magnitude of the convection heat transfer coefficient ( $h$ ) is appeared to be slightly larger at  $\phi = 3\%$  when compared to  $\phi = 0\%$ . However, due to the height adjustment (here height increases for  $\phi = 3\%$ ) to keep the  $Ra_{nl}$  constant for all  $\phi$ s, the thermal conductance (i.e., surface area of the enclosure  $\times$  convection heat transfer coefficient) must be even larger at  $\phi = 3\%$  when compared to  $\phi = 0\%$  situation, which will guarantee higher heat transfer rate. Therefore,  $Nu_n$ -time profiles alone do not give a complete conclusion on the influence on nanoparticles on Nusselt number.

Additionally, at a given time, the magnitude of  $Nu_n$  is higher at higher  $Ra_{nl}$  as expected.  $Nu_n$ -time profile requires more time to reach its last asymptote (i.e.,  $Nu_n \rightarrow 0$ ; the thermal equilibrium point) when  $Ra_{nl}$  is higher.

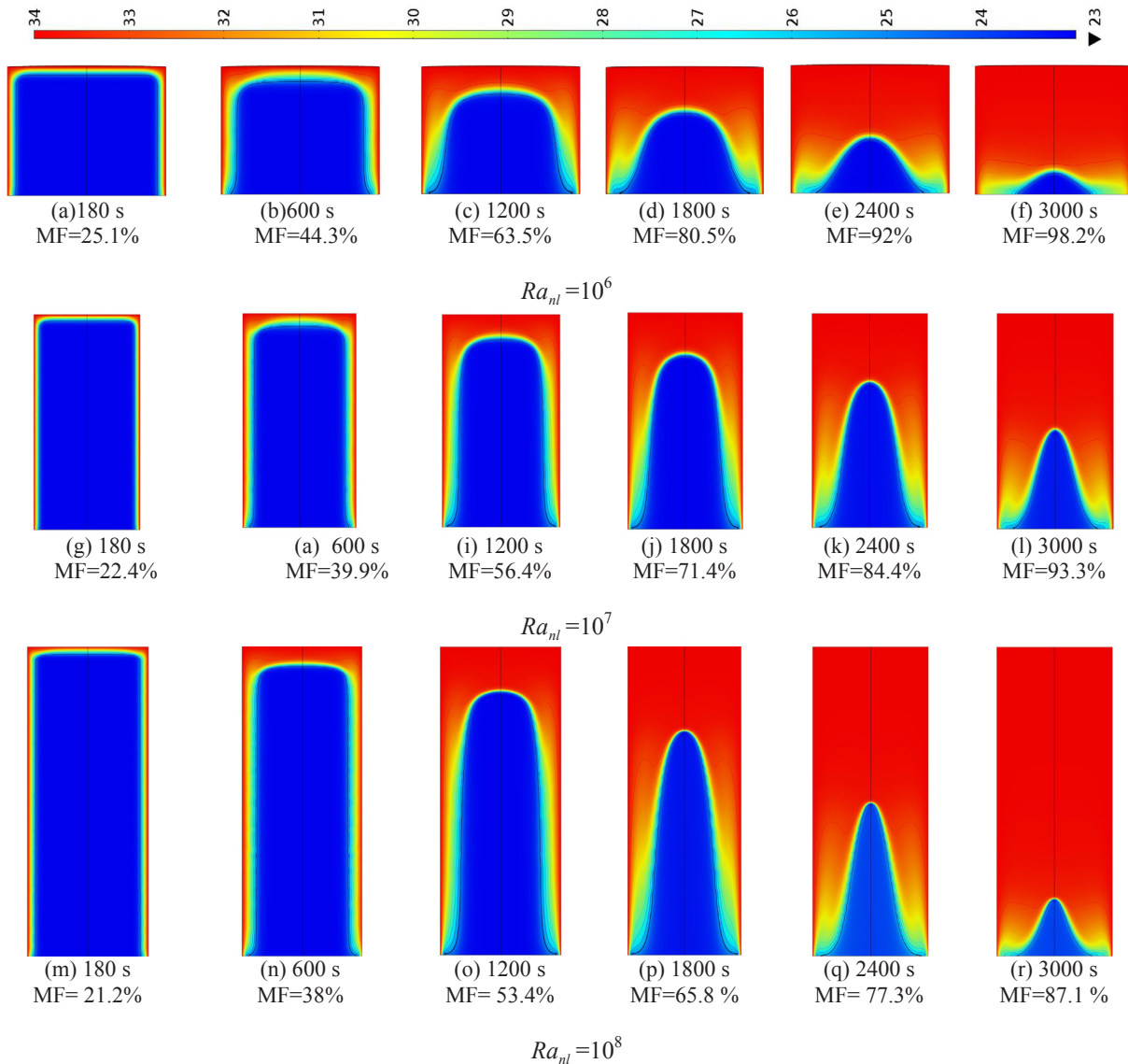


Fig. 5b. Effect of different  $Ra_{nl}$  on the melting progression at the same time for a given  $\phi = 3\%$ .

### 3.3. Energy stored

Fig. 8 presents energy stored inside the C-TES system with time for selected values of volume fraction of nanoparticles and Rayleigh number. For  $\phi = 0, 3\%$ , and  $5\%$ , the transient variation in the energy stored is presented at  $Ra_l = 10^6$ . Two additional profiles, representing  $Ra_{nl} = 10^6$  at  $\phi = 3\%$  and  $5\%$ , are presented as well for comparison purpose. Focusing on a single profile of transient variation in the energy stored given in Fig. 8 (e.g.,  $Ra_l = 10^6$  and  $\phi = 0\%$ ), it is observed that stored energy increases from zero to a maximum value as time advances during the melting process. However, the rate of energy stored is initially high which can be confirmed from the high slope of the profile at the beginning of the melting process. The relatively higher magnitude of the temperature gradient at the early stage of melting (i.e., in the conduction regime) assists transfer of larger amounts of energy and subsequently storing it. A change in the slope of the profile is observed near the time where transition melting regime (i.e., the conduction + convection melting regime) is evolved. From this point onward, energy is stored with an almost linearly increasing trend as time passes through the remaining transition regime and most part of convection with shrinking solid regime. Towards the end of melting, the rate of the stored energy decreases to its minimum where the maximum

degradation of the temperature gradient occurs as the thermal equilibrium is achieved inside the enclosure.

At the beginning of the melting process, where a large portion of the enclosure is filled with solid nano-PCM, stored energy primarily depends on the specific heat capacity of solid nano-PCM, i.e.,  $(\rho C_p)_{ns}$ . The improvement of this specific heat capacity with increasing  $\phi$  is nearly insignificant; for example, a 0.06% increase of  $(\rho C_p)_{ns}$  is calculated when  $\phi$  is changed from 0% to 5%. Therefore, almost no variation is observed in the energy stored profiles at different  $\phi$  in the conduction regime of melting. From the thermophysical property values, it can be shown that the specific heat capacity of liquid nano-PCM  $(\rho C_p)_{nl}$  increases with increasing  $\phi$ , while the latent heat capacity  $(\rho h_{nl})$  of nano-PCM decreases with increasing  $\phi$ . Therefore, beyond the conduction regime of melting, storing energy inside the enclosure largely depends on specific heat capacities of solid and liquid nano-PCMs, latent heat capacity, and the relative magnitudes of these heat capacity values, respectively. Overall, increasing  $\phi$  slightly decreases total energy stored inside the enclosure given that the size of the enclosure is unchanged (i.e., Rayleigh number is defined at base properties). Note that the size of the C-TES system should be increased to keep the  $Ra_{nl}$  constant with increasing  $\phi$ . Therefore, due to the enlarged size, total energy stored in the C-TES system at  $Ra_{nl} = 10^6$  is higher than at  $Ra_l = 10^6$  when  $\phi$  is

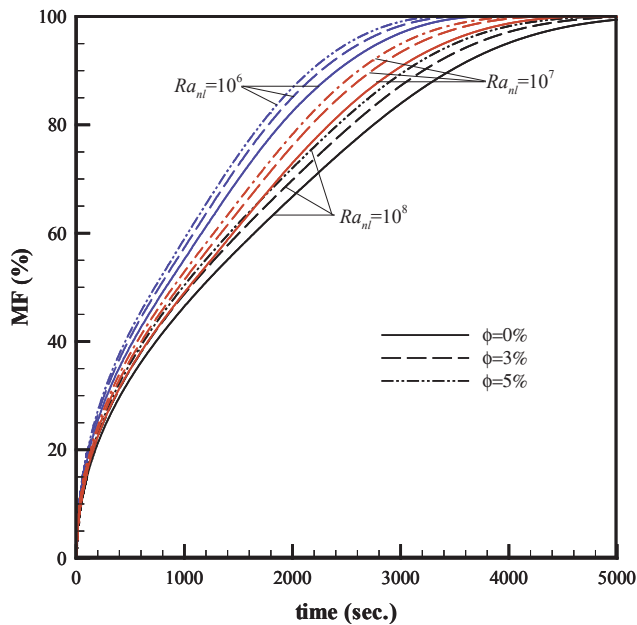


Fig. 6. Comparison of melting fraction between different volume fractions of nanoparticles ( $\phi = 0, 3, \text{ and } 5\%$ ) and  $Ra_{ni} = 10^6, 10^7, \text{ and } 10^8$ .

Table 9

MF and its increment by dispersing of nanoparticles at 300 s.

	$Ra_{ni} = 10^6$	$Ra_{ni} = 10^7$	$Ra_{ni} = 10^8$
$\phi = 0\%$	30.7% (0.0%)	27.3% (0.0%)	25.8% (0.0%)
$\phi = 3\%$	32% (+4.2%)	28.7% (+5.1%)	27.1% (+5%)
$\phi = 5\%$	32.9% (+7.1%)	29.6% (+8.4%)	28% (+8.5%)

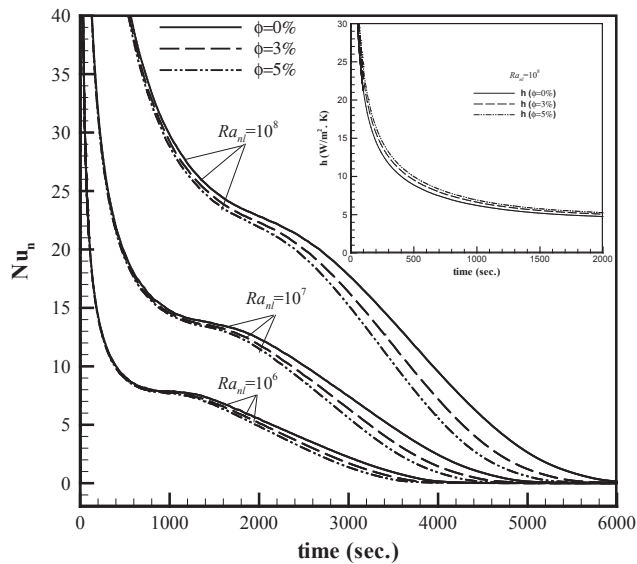


Fig. 7. Comparison of average Nusselt number based on  $k_{nf}$  for  $\phi = 0, 3, \text{ and } 5\%$ ,  $Ra_{ni} = 10^6, 10^7, \text{ and } 10^8$ .

constant.

Fig. 9 illustrates energy stored inside the C-TES system with time for a given value of  $\phi$  at  $Ra_{ni}$  of  $10^6, 10^7, \text{ and } 10^8$ , respectively. A general trend of increased energy stored at larger Rayleigh number is observed. A higher slope is observed at larger Rayleigh number which is expected due to the larger amount of heat transfer through the wall. Very high energy storage is observed initially which approaches an almost steady value later when melting process is dominated by natural convection

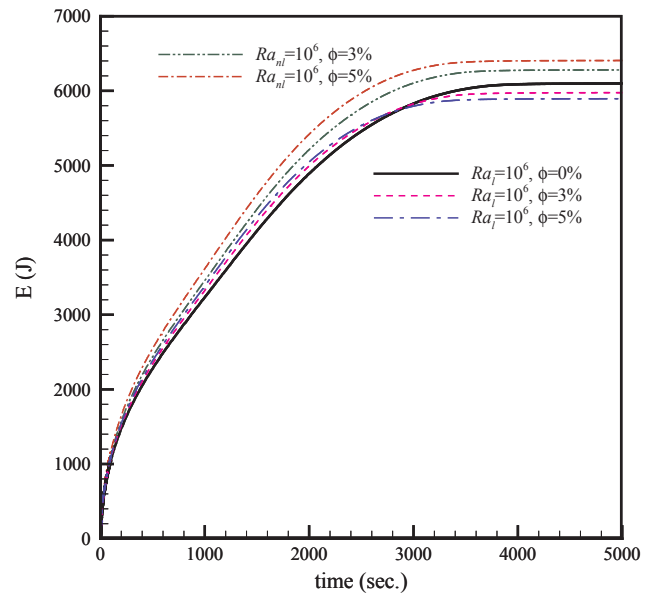


Fig. 8. Comparison of total energy stored inside the C-TES system for different volume fractions of nanoparticles ( $\phi = 0, 3, \text{ and } 5\%$ ) and  $Ra_{ni}, Ra_l = 10^6$ .

for all the three selected values of Rayleigh number. The difference in energy stored with Rayleigh number is less during the beginning of the melting; as melting reaches the convection dominated regime, a larger difference is observed due to increased melting with Rayleigh number in convection regime.

### 3.4. Comparison with experiments

In this section, some selected results obtained from the current numerical simulations are compared to the results obtained from subsequent experimental analyses. For this purpose, an experimental setup is constructed to perform the melting experiment and images are captured during the melting process of the nano-PCM inside the C-TES system. A schematic diagram of the complete experimental setup is presented in Fig. 10a. The setup consists of an acrylic water tank, which is insulated from all sides except one for visualization, a water heater

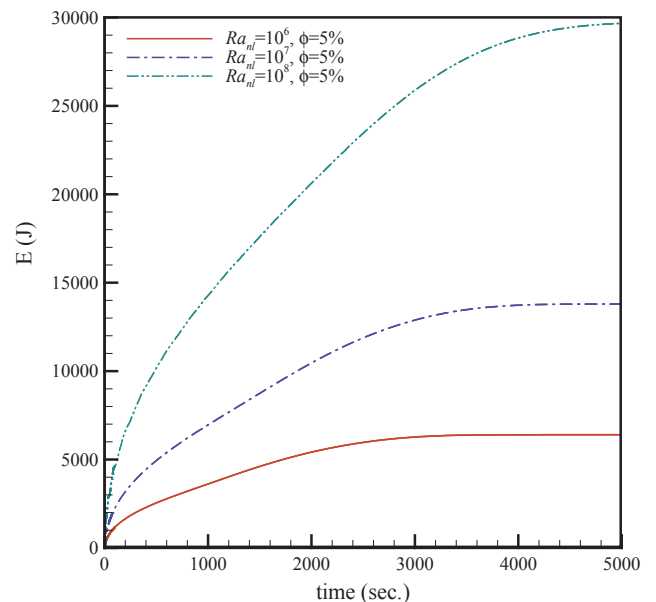


Fig. 9. Comparison of total energy stored inside the C-TES system for different  $Ra_{ni} (= 10^6, 10^7, \text{ and } 10^8)$  and  $\phi = 5\%$ .

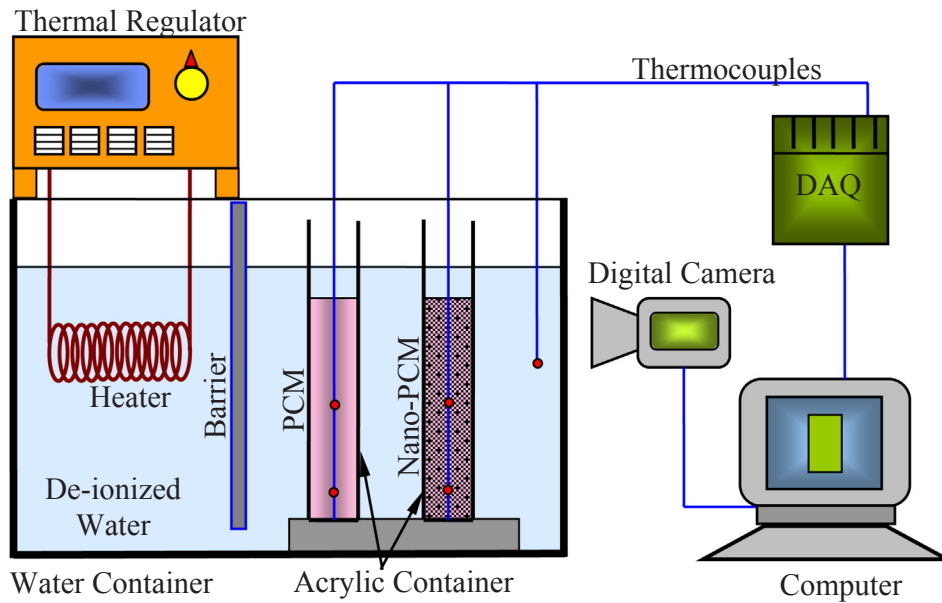


Fig. 10a. Schematic diagram of the experimental setup used for visualization.

equipped with a circulatory pump, a digitally controlled thermal regulator, T-type thermocouples, and a 16-channel DAQ system. The acrylic tank is divided into two parts by using a barrier to avoid the intensity of the water circulation and turbulent effect caused by the circulatory pump. To have a better background for capturing the images during the melting process, one side of the barrier where nano-PCM located in front of that was painted white, while the other side was painted black for the pure PCM. A 5 cm clearance is maintained between the bottom of the acrylic water tank and lower part of the barrier. Melting experiments are performed on both PCM and nano-PCM simultaneously to ensure exactly same experimental environment and to avoid any discrepancy due to the change in minor environmental condition. To ensure this, two vertical C-TES systems are constructed by using acrylic pipes with inner diameters of 4.44 cm and thicknesses of 0.3 cm. These two enclosures are insulated from the bottom and vertically attached to a 2.5 cm thick acrylic plate by using transparent acrylic cement. The center-to-center distance between the two enclosures is 14 cm. To prepare the nano-PCM, 50 mg of copper oxide nanoparticles are dispersed into 350 ml of molten coconut oil at the

temperature of 60 °C. To ensure the homogeneity of the mixture, it is stirred by a magnetic stirrer (model: SP88854100, manufacturer: Thermo Scientific) initially for 12 h. Then an ultrasound sonicator (model: Q500, manufacturer: Qsonica) is used to improve the homogeneity of the mixture further, to minimize the sedimentation, and to release the trapped air inside the nano-PCM. Subsequently, one enclosure is filled with  $H = 8.5$  cm of nano-PCM ( $Ra_{nl} = 1.3 \times 10^7$ ), while the other enclosure is filled with  $H = 8.6$  cm of pure PCM ( $Ra_{nl} = 1.35 \times 10^7$ ). It is worth mentioning that visualization process becomes increasingly difficult for the nano-PCM, specifically at higher values of  $\phi$ , due to its dark black color. Therefore, a relatively lower value of  $\phi$  is selected as our intention is to make a comparison of melting images obtained from numerical simulation and experimental visualization (see Fig. 10b).

The PCM and nano-PCM-filled enclosures are put inside a constant temperature bath where water is maintained at 21 °C using a low temperature thermal regulator. Subsequently, multiple melting and solidification processes are conducted to ensure the stability of the mixture and to release the trapped air inside the PCM and nano-PCM.

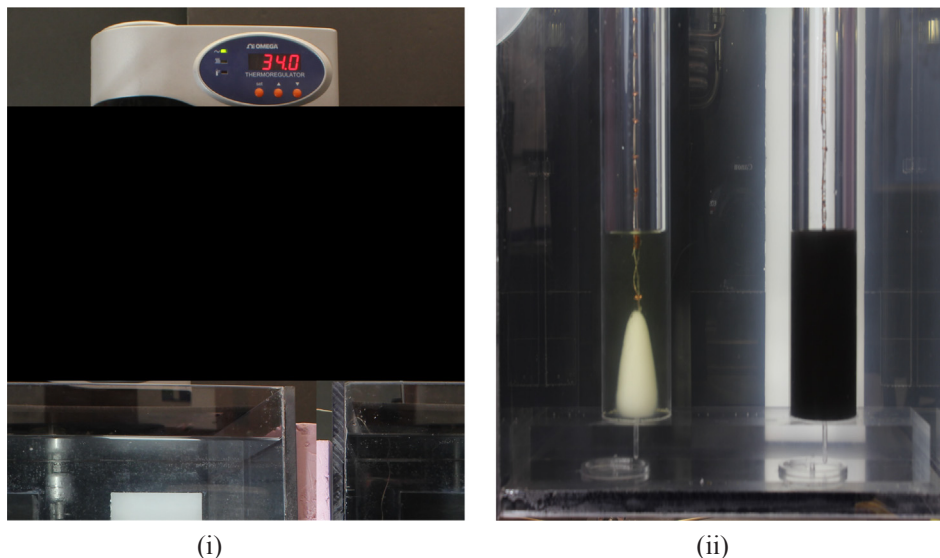


Fig. 10b. Experimental setup: (i) Constant temperature bath (ii) C-TES system inside the constant temperature bath during the melting process.

Next, the enclosures are placed inside the acrylic water tank where the temperature of the water is elevated and maintained at 34 °C (10 °C above the  $T_m$ ) to initiate the melting process. To ensure the isothermal boundary condition inside the acrylic water tank, T-type thermocouples were placed at the top and bottom of the acrylic water tank, which monitored the temperature of the water every 10 s. A digital camera is used to capture images periodically (i.e. every 60 s) to track the liquid-solid interface during the melting process. For eight selected times, images obtained from numerical simulation and experimental

visualization are presented and compared in Fig. 11 for pure PCM and Fig. 12 for nano-PCM, respectively. Corresponding melting fractions are presented as well. The selected images cover almost the entire range of melting regimes, which exhibit the different characteristic features of the melting process as given below:

(a) Images at  $t = 180$  and 600 s: At these time intervals, the solid-liquid interface is parallel to the walls, a pattern resembles the conduction dominated melting process as discussed earlier. By comparing the

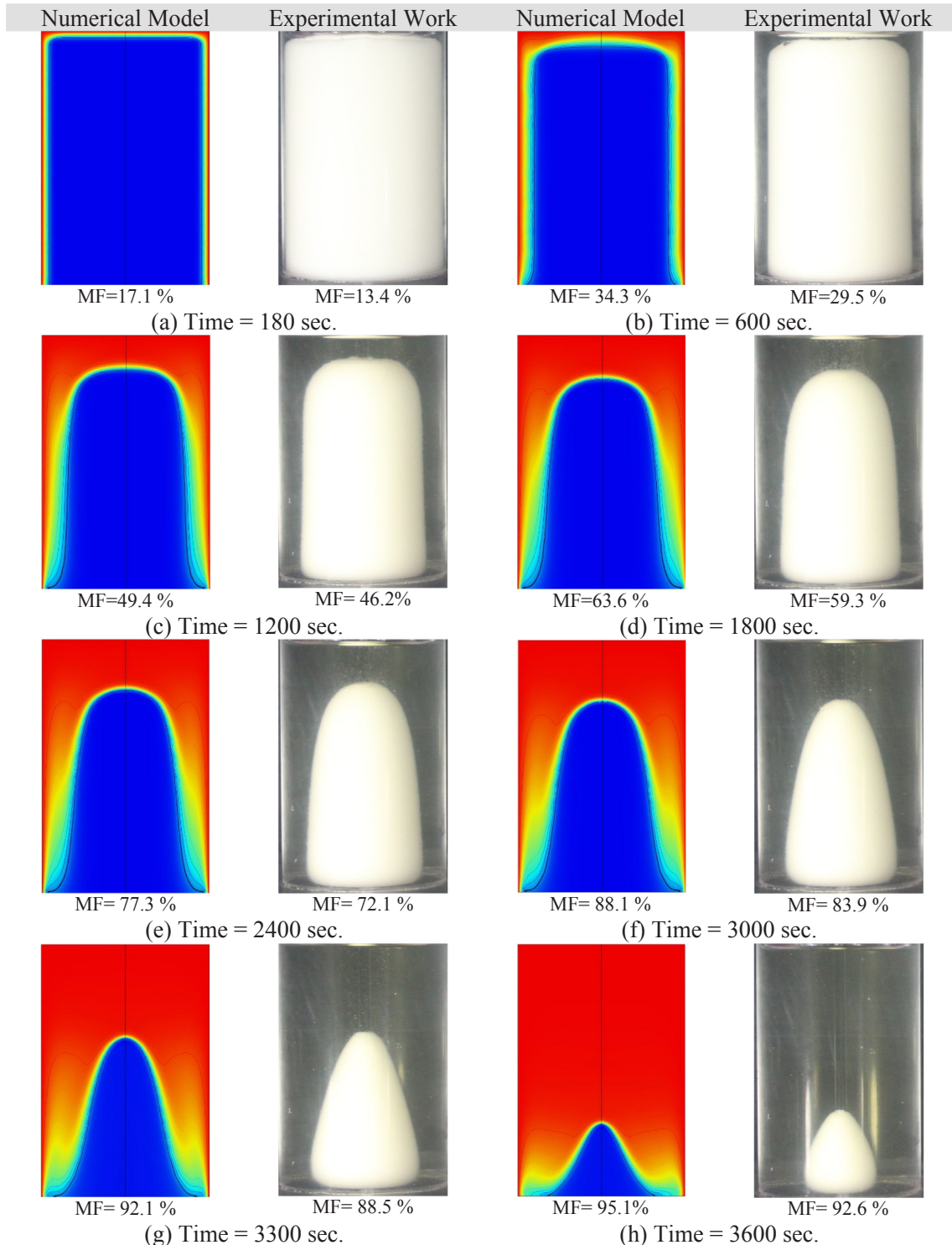


Fig. 11. Melting visualization comparison between numerical and experimental works for pure PCM,  $Ra_{nl} = 1.35 \times 10^7$ , and  $H = 8.6$  cm.

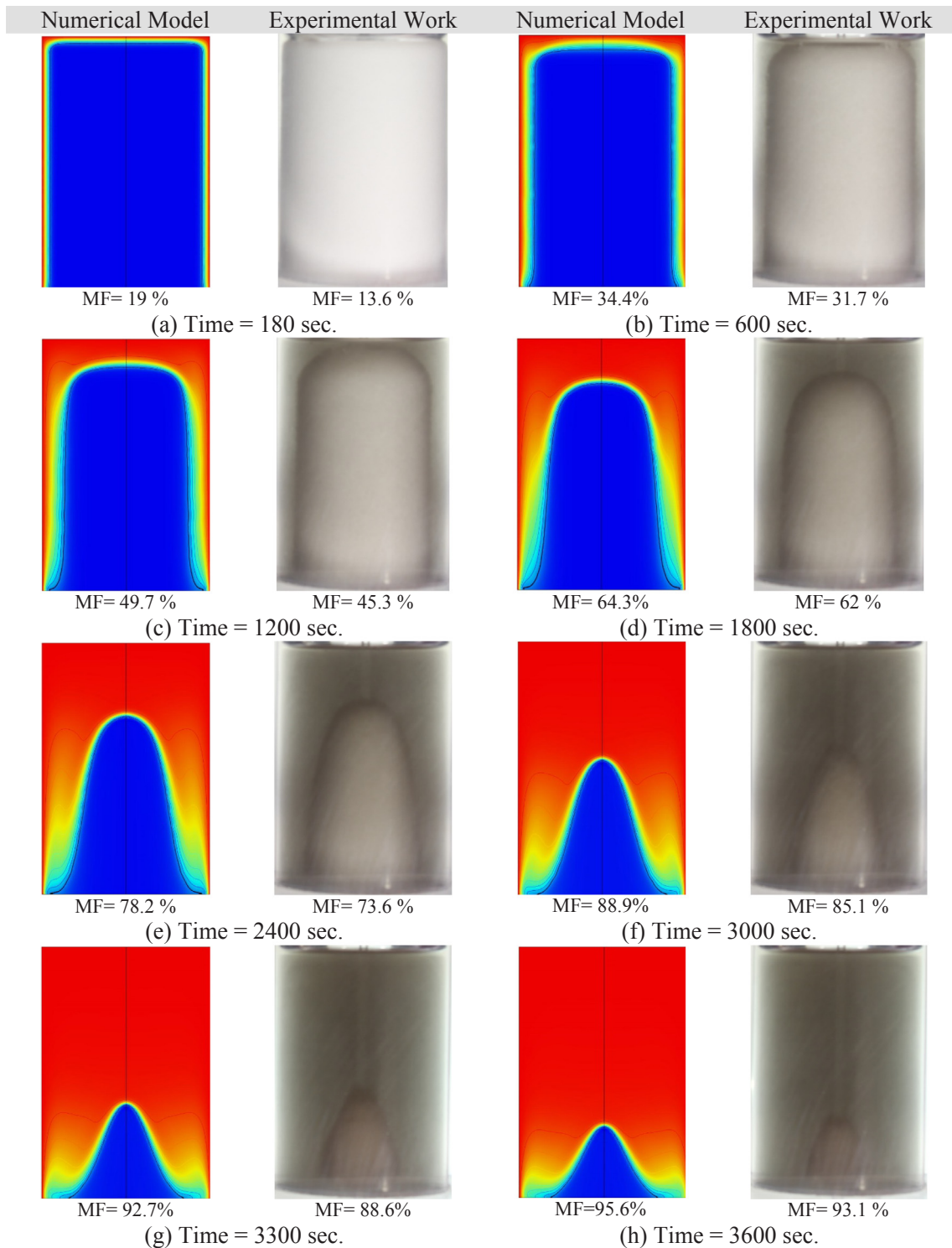


Fig. 12. Melting visualization comparison between present numerical and experimental works for nano-PCM (0.05 g CuO + 350 ml coconut oil),  $Ra_{nl} = 1.3 \times 10^7$ , and  $H = 8.5$  cm.

numerical model and experimental images, an almost identical pattern can be observed. However, the thickness of the liquid PCM or nano-PCM layer close to the lateral walls in numerical simulation seems to be slightly larger than the experimental images. The top part of the remaining solid PCM/nano-PCM is slightly more curved for the numerical work. The numerical model showed a higher melting fraction for both pure PCM and nano-PCM.

(b) Images at  $t = 1200$  and  $1800$  s: At these time intervals, the warm liquid PCM/nano-PCM starts to move upward as the buoyancy

forces overcome the viscous forces. Higher temperature liquid PCM/nano-PCM are accumulated at the top due to the thermal stratification effect. As a result, the remaining solid PCM/nano-PCM resembles a dome shape. A slightly flatter curvature at the top can be observed in the numerical work for both PCM/nano-PCM. As it can be seen from the melting fraction values under each image, the magnitude of the numerically obtained melting fractions are higher than the experimentally obtained values.

(c) Images at  $t = 2400$  and  $3000$  s: As natural convection develops, the

remaining solid part tends to have an inverted paraboloid shape. For the pure PCM, the experimental images show a sharper curvature at the top than numerical work. However, an opposite behavior exists at the same time for nano-PCM. At these time intervals, the discrepancy of the melting fraction between numerical models and experimental work increases.

- (d) Images at  $t = 3300$  and  $3600$  s: Most discrepancy in the melting pattern between numerical models and experimental works is seen here. A sharper curvature at the top of the remaining solid PCM/nano-PCM is observed.

In general, a good agreement between numerical result and experimental work is achieved. However, there are some discrepancies observed in melting pattern and melting fraction. Several factors can possibly be the reasons for such discrepancies. One of the possible major factors is the conduction resistance due to finite thickness of the acrylic pipe, which is ignored during numerical simulation. This resistance may reduce heat transfer rate slightly in the experimental work even though the outer surface temperature is kept constant in both the numerical simulation and the experiment work. In addition to that, in the experimental work an expansion of the nano-PCM is seen in the enclosure during melting process. However, this phenomenon is ignored in the numerical model. Other minor factors may include the difference between the thermophysical properties based on property models and exact property values, heat loss through the bottom of the enclosure, and minor water temperature fluctuations in the acrylic tank. Table 10 shows the difference between melting fraction calculated by the numerical model and experimental work for pure PCM and nano-PCM as it is discussed earlier in this section (i.e. Figs. 11 and 12). It should be noted that the melting fractions of the images obtained from experimental work are calculated by using the Grafula software and based on the image processing method as it was also used in [54]. To do so, a curvature was fitted to the solid-liquid interface for the nano-PCM/PCM by tracing the solid-liquid interface line using cursor. At the next step, the coordination of each point located at the solid-liquid interface was extracted. Finally, according to the dimensions of the C-TES system and Eq. (19), the melting fractions for nano-PCM and pure PCM at different time intervals were obtained.

### 3.5. Uncertainty analysis of the experimental work

In this section, the uncertainty analysis of experimental work used to validate the numerical results is presented. These uncertainties could be associated to two stages including (i) maintaining isothermal boundary conditions before and during performing experiment (i.e. maintaining the initial temperature of  $21\text{ }^{\circ}\text{C}$  and  $34\text{ }^{\circ}\text{C}$  during the experiment) and (ii) processing the melting fractions for images obtained from experimental work. The accuracies of the thermal regulators used in the experimental work are shown in Table 11.

Other uncertainty could be associated with the calculations of the melting fraction using Grafula software. As it is mentioned earlier in the Section 3.4, the calculations are based fitting a curvature to the solid-

**Table 11**  
Uncertainty analysis of experimental work.

Equipment	Accuracy ( $U_a$ )	Measured values ( $x$ )	Relative uncertainty ( $U_c/x$ )
T-type omega thermocouples	$\pm 1\text{ }[^{\circ}\text{C}]$	$21\text{ }^{\circ}\text{C}$ $34\text{ }^{\circ}\text{C}$	$\pm 4.7\%$ $\pm 2.9\%$
Omega Heater (HCTB-3020)	$\pm 0.01\text{ }[^{\circ}\text{C}]$	$34\text{ }^{\circ}\text{C}$	$\pm 0.03\%$
Cole-Parmer Polystat (CR250WU)	$\pm 0.1\text{ }[^{\circ}\text{C}]$	$21\text{ }^{\circ}\text{C}$	$\pm 0.47\%$

liquid interface by moving the cursor along the solid-liquid interface. Hence, the human error could cause an uncertainty at this stage. By repeating this approach and comparing the obtained melting fraction at different time intervals multiple times, it was seen that there is less than  $\pm 5\%$  error associated with such calculation.

## 4. Conclusion

The melting process, heat transfer and energy storage characteristics of a bio-based nano-PCM in a C-TES system are numerically investigated and verified with experimental work. The C-TES system is assumed to be filled with copper oxide nanoparticles dispersed in coconut oil at different volume fractions of nanoparticles ( $\phi$ ) and different Rayleigh numbers ( $Ra_{nl}$ ). The modeling results are compared with previously published numerical and experimental works and a good agreement is achieved. The following conclusion can be drawn from the obtained results:

- Initially, the melting process is dominated by conduction. As time advances, the buoyancy force can overcome the viscous force, resulting in a gradual increase in the domination of natural convection melting. For a certain period, mixed conduction and convection remain dominant mode of melting, while the influence of the conduction diminishes with time. Subsequently, the melting process is dominated by convection while the height of the solid nano-PCM shrinks as time advances. The shape of the remaining solid nano-PCM is controlled by these regimes at each stage.
- Adding copper oxide nanoparticles to coconut oil does not show a significant effect on the melting rate at the early stages of melting process. However, as time advanced, dispersion of copper oxide nanoparticles to coconut oil improves the melting rate in the PCM.
- The magnitude of the Nusselt number is higher at the initial stages of the melting process due to the relatively high temperature gradient and a high heat flux at this stage. Nusselt number drops sharply from a large value in the conduction regime as time advances. A change in slope in the Nusselt number profile is an indication of the formation of thermal boundary layer and the initiation of the convection. This slope change strongly depends on the Rayleigh number. A fully convection dominated regime does not exist, instead convection dominated melting occurs in parallel with

**Table 10**

A comparison between melting fraction (%) calculation by numerical model and experimental work.

Time (s)	Pure PCM			Nano-PCM		
	Numerical	Experimental	Difference (%)	Numerical	Experimental	Difference (%)
180	17.1	13.4	21.6	19	13.6	28.4
600	34.3	29.5	13.9	34.4	31.7	7.8
1200	49.4	46.2	6.4	49.7	45.3	8.8
1800	63.6	59.3	6.7	64.3	62	3.5
2400	77.3	72.1	6.7	78.2	73.6	5.8
3000	88.1	83.9	4.7	88.9	85.1	4.2
3300	92.1	88.5	3.9	92.7	88.6	4.4
3600	95.1	92.6	2.6	95.6	93.1	2.6

the shrinking solid nano-PCM. Nano-PCMs with higher volume fractions of nanoparticles exhibit larger convection heat transfer coefficients.

- Increasing volume fractions of nanoparticles decreases total energy stored inside the C-TES system given that the size of the enclosure is unchanged (i.e., Rayleigh number is defined at base properties). However, opposite nature in the energy storage rate is observed if the Rayleigh number is defined based on nano-PCM properties.
- Finally, numerically obtained solid-liquid interface locations and melt fractions for base PCM and nano-PCM are compared with experimental results and a very good agreement is obtained which gives confidence in the obtained numerical results.
- Both melting and solidification processes are equally important for the TES system performance. In the subsequent studies, solidification process inside a cylindrical TES will be performed and the effect of addition of nanoparticles will be examined to have a better understanding of the effect of addition of nanoparticles on both melting and solidification processes in a cylindrical TES system.

## References

- [1] Batley SL, Colbourne D, Fleming PD, Urwin P. Citizen versus consumer: challenges in the UK green power market. *Energy Policy* 2001;29:479–87.
- [2] Fuss S, Johansson JA, Szolgayova J, Obersteiner M. Impact of climate policy uncertainty on the adoption of electricity generating technologies. *Energy Policy* 2009;37:733–43.
- [3] Georgakellos D. Impact of a possible environmental externalities internalization on energy prices: the case of the greenhouse gases from the Greek electricity sector. *Energy Econ* 2009;32:202–9.
- [4] Longo A, Markandya A, Petrucci M. The internalization of externalities in the production of electricity: willingness to pay for the attributes of a policy for renewable energy. *Ecol Econ* 2008;67:140–52.
- [5] Dhaidan NS, Khodadadi JM. Melting and convection of phase change materials in different shape containers: a review. *Renew Sustain Energy Rev* 2015;43:449–77.
- [6] Dhaidan NS. Nanostructures assisted melting of phase change materials in various cavities. *Appl Therm Eng* 2017;111:193–212.
- [7] Khan Z, Khan Z, Ghafoor A. A review of performance enhancement of PCM based latent heat storage system within the context of materials, thermal stability and compatibility. *Energy Convers Manage* 2016;115:132–58.
- [8] Zalba B, Marin J, Cabeza LF, Mehling H. A review on thermal energy storage with phase change materials: heat transfer analysis and applications. *Appl Therm Eng* 2003;23:251–83.
- [9] Dhaidan NS, Khodadadi JM, Al-Hattab TA, Al-Mashat SM. Experimental and numerical investigation of melting of phase change material/nanoparticle suspensions in a square container subjected to a constant heat flux. *Int J Heat Mass Transf* 2013;66:672–83.
- [10] Zeng Y, Fan L, Xiao Y, Yu Z, Cen K. An experimental investigation of melting of nanoparticle-enhanced phase change materials (NePCMs) in a bottom heated vertical cylindrical cavity. *Int J Heat Mass Transf* 2013;66:111–7.
- [11] Fan L, Khodadadi JM. Thermal conductivity enhancement of phase change materials for thermal energy storage: a review. *Renew Sustain Energy Rev* 2011;15:24–46.
- [12] Ibrahim NI, Al-Sulaiman FA, Rahman S, Yilbas BS, Sahin AZ. Heat transfer enhancement of phase change materials for thermal energy storage applications: a critical review. *Renew Sustain Energy Rev* 2017;74:26–50.
- [13] Jourabian M, Farhadi M, Rabiataj Darzi A. Constrained ice melting around one cylinder in horizontal cavity accelerated using three heat transfer enhancement techniques. *Int J Therm Sci* 2018;125:231–47.
- [14] Khodadadi JM, Fan L, Babaei H. Thermal conductivity enhancement of nanostructure-based colloidal suspensions utilized as phase change materials for thermal energy storage: a review. *Renew Sustain Energy Rev* 2013;24:418–44.
- [15] Zhang X, Chen X, Han Z, Xu W. Study on phase change interface for erythritol with nano-copper in spherical container during heat transport. *Int J Heat Mass Transf* 2016;92:490–6.
- [16] Hossain R, Mahmud S, Dutta A, Pop I. Energy storage system based on nanoparticle-enhanced phase change material inside porous medium. *Int J Therm Sci* 2015;91:49–58.
- [17] Sparrow EM, Broadbent JA. Inward melting in a vertical tube which allows free expansion of the phase-change medium. *ASME J Heat Transf* 1982;104:309–15.
- [18] Wenzhen C, Shangmo C, Zhen L, Wangmin G. Study of contact melting inside isothermally heated vertical cylindrical capsules. *J Therm Sci* 1993;2:190–5.
- [19] Wu YK, Lacroix M. Melting of a PCM inside a vertical cylindrical capsule. *Int J Numer Meth Fluids* 1995;20:559–72.
- [20] Jones BJ, Sun D, Krishnan S, Garimella SV. Experimental and numerical study of melting in a cylinder. *Int J Heat Mass Transf* 2006;49:2724–38.
- [21] Shmueli H, Ziskind G, Letan R. Melting in a vertical cylindrical tube: numerical investigation and comparison with experiments. *Int J Heat Mass Transf* 2010;53:4082–91.
- [22] Wu S, Wang H, Xia S, Zhu D. Numerical simulation on thermal energy storage behavior of cu/paraffin nanofluids PCMs. *Proc Eng* 2012;31:240–4.
- [23] Sciacovelli A, Colella F, Verda V. Melting of PCM in a thermal energy storage unit: Numerical investigation and effect of nanoparticle enhancement. *Int J Energy Res* 2013;37:1610–23.
- [24] Fan L, Zhu Z, Zeng Y, Lu Q, Yu Z. Heat transfer during melting of graphene based composite phase change materials heated from below. *Int J Heat Mass Transf* 2014;79:94–104.
- [25] Alshaer WG, Nada SA, Rady MA, Del Barrio EP, Sommier A. Thermal management of electronic devices using carbon foam and PCM/nano-composite. *Int J Therm Sci* 2015;89:79–86.
- [26] Das N, Takata Y, Kohno M, Harish S. Effect of carbon nano inclusion dimensionality on the melting of phase change nanocomposites in vertical shell-tube thermal energy storage unit. *Int J Heat Mass Transf* 2017;113:423–32.
- [27] Bechiri M, Mansouri K. Analytical study of heat generation effects on melting and solidification of nano-enhanced PCM inside a horizontal cylindrical enclosure. *Appl Therm Eng* 2016;104:779–90.
- [28] Mahdi JM, Nsofor EC. Solidification of a PCM with nanoparticles in triplex-tube thermal energy storage system. *Appl Therm Eng* 2016;108:596–604.
- [29] Abdulateef AM, Mat S, Abdulateef J, Sopian K, Al-Abidi AA. Thermal performance enhancement of triplex tube latent thermal storage using fins-nano-phase change material technique. *Heat Transf Eng* 2017:1–14.
- [30] Pahamli Y, Hosseini MJ, Ranjbar AA, Bahrampoury R. Effect of nanoparticle dispersion and inclination angle on melting of PCM in a shell and tube heat exchanger. *J Taiwan Inst Chem Eng* 2017;81:316–34.
- [31] Parsazadeh M, Duan X. Numerical and statistical study on melting of nanoparticle enhanced phase change material in a shell-and-tube thermal energy storage system. *Appl Therm Eng* 2017;111:950–60.
- [32] Mahdi JM, Nsofor EC. Melting enhancement in triplex-tube latent thermal energy storage system using nanoparticles-fins combination. *Int J Heat Mass Transf* 2017;109:417–27.
- [33] Parsazadeh M, Duan X. Numerical study on the effects of fins and nanoparticles in a shell and tube phase change thermal energy storage unit. *Appl Energy* 2018;216:142–56.
- [34] Motahar S, Alemrajabi AA, Khodabandeh R. Experimental study on solidification process of a phase change material containing TiO<sub>2</sub> nanoparticles for thermal energy storage. *Energy Convers Manage* 2017;138:162–70.
- [35] Arici M, Tutuncu E, Kan M, Karabay H. Melting of nanoparticle-enhanced paraffin wax in a rectangular enclosure with partially active walls. *Int J Heat Mass Transf* 2017;104:7–17.
- [36] Motahar S, Alemrajabi AA, Khodabandeh R. Experimental investigation on heat transfer characteristics during melting of a phase change material with dispersed TiO<sub>2</sub> nanoparticles in a rectangular enclosure. *Int J Heat Mass Transf* 2017;109:134–46.
- [37] Al-Jethelah M, Tasmim SH, Mahmud S, Dutta A. Melting of nano-PCM in an enclosed space: scale analysis and heatline tracking. *Int J Heat Mass Transf* 2018;119:841–59.
- [38] Sharma S, Micheli L, Chang W, Tahir AA, Reddy KS, Mallick TK. Nano-enhanced phase change material for thermal management of BICPV. *Appl Energy* 2017;208:719–33.
- [39] Al-Waeli AHA, Sopian K, Chaichan MT, Kazem HA, Ibrahim A, Mat S, et al. Evaluation of the nanofluid and nano-PCM based photovoltaic thermal (PVT) system: an experimental study. *Energy Convers Manage* 2017;151:693–708.
- [40] Bahiraei F, Fartaj A, Nazri GA. Experimental and numerical investigation on the performance of carbon-based nanoenhanced phase change materials for thermal management applications. *Energy Convers Manage* 2017;153:115–28.
- [41] Hosseinzadeh M, Sardarabadi M, Passandideh-Fard M. Energy and exergy analysis of nanofluid based photovoltaic thermal system integrated with phase change material. *Energy* 2018;147:636–47.
- [42] Choi S, Kim S, Lee T, Hahn D. Computation of the natural convection of nanofluid in a squared cavity with homogeneous and nonhomogeneous models. *Num Heat Transf* 2014;65:287–301.
- [43] Jang SP, Choi SU. Effects of various parameters on nanofluid thermal conductivity. *ASME J. Heat Transf* 2007;129:617–23.
- [44] Bejan A. *Convection heat transfer*. New York: Wiley; 2013.
- [45] Khodadadi JM, Hosseinzadeh SF. Nanoparticle-enhanced phase change materials (NEPCM) with great potential for improved thermal energy storage. *Int Commun Heat Mass Transf* 2007;34:534–43.
- [46] Hosseinzadeh SF, Rabiataj Darzi AA, Tan FL. Numerical investigations of unconstrained melting of nano-enhanced phase change material (NEPCM) inside a spherical container. *Int J Therm Sci* 2012;51:77–83.
- [47] Dhaidan NS, Khodadadi JM, Al-Hattab TA, Al-Mashat SM. Experimental and numerical investigation of melting of NePCM inside an annular container under a constant heat flux including the effect of eccentricity. *Int J Heat Mass Transf* 2013;67:455–68.
- [48] Dhaidan NS, Khodadadi JM, Al-Hattab TA, Al-Mashat SM. Experimental and numerical study of constrained melting of n-octadecane with CuO nanoparticle dispersions in a horizontal cylindrical capsule subjected to a constant heat flux. *Int J Heat Mass Transf* 2013;67:523–34.
- [49] Groulx D, Biwole PH. Solar PV passive temperature control using phase change materials. In: *Proceedings of the 15th international heat transfer conference, IHTC-15, August 10–15, Kyoto, Japan; 2014.*
- [50] Xu Y, Li M, Zheng Z, Xue X. Melting performance enhancement of phase change material by a limited amount of metal foam: configurational optimization and economic assessment. *Appl Energy* 2018;212:868–80.
- [51] Ho CJ, Gao JY. An experimental study on melting heat transfer of paraffin dispersed with Al<sub>2</sub>O<sub>3</sub> nanoparticles in a vertical enclosure. *Int J Heat Mass Transf*

- 2013;62:2–8.
- [52] Hosseinizadeh SF, Darzi AAR, Tan FL. Numerical investigations of unconstrained melting of nano-enhanced phase change material (NEPCM) inside a spherical container. *Int J Therm Sci* 2012;51:77–83.
- [53] Li T, Lee J, Wang R, Tae Kang Y. Heat transfer characteristics of phase change nanocomposite materials for thermal energy storage application. *Int J Heat Mass Transf* 2014;75:1–11.
- [54] Tan FL. Constrained and unconstrained melting inside a sphere. *Int Commun Heat Mass Transf* 2008;35:466–75.